Cellular/Molecular

A Pathogenic Missense Mutation in Kainate Receptors Elevates Dendritic Excitability and Synaptic Integration through Dysregulation of SK Channels

Toshihiro Nomura,[1] Sakiko Taniguchi,[2] Yi-Zhi Wang,[3] Nai-Hsing Yeh,[1] Anika P. Wilen,[3] Charlotte C.M. Castillon,[1] Kendall M. Foote,[2] Jian Xu,[1] John N. Armstrong,[1] Jeffrey N. Savas,[3] Geoffrey T. Swanson,[2,5] and Anis Contractor[1,4,5]

[1]Department of Neuroscience, Feinberg School of Medicine, Northwestern University, Chicago, Illinois 60611, [2]Department of Pharmacology, Feinberg School of Medicine, Northwestern University, Chicago, Illinois 60611, [3]Department of Neurology, Feinberg School of Medicine, Northwestern University, Chicago, Illinois 60611, [4]Department of Psychiatry and Behavioral Sciences Feinberg School of Medicine, Northwestern University, Chicago, Illinois 60611, and [5]Department of Neurobiology, Weinberg College of Arts and Sciences Northwestern University, Chicago, Illinois 60611

Numerous rare variants that cause neurodevelopmental disorders (NDDs) occur within genes encoding synaptic proteins, including ionotropic glutamate receptors. However, in many cases, it remains unclear how damaging missense variants affect brain function. We determined the physiological consequences of an NDD causing missense mutation in the *GRIK2* kainate receptor (KAR) gene, that results in a single amino acid change p.Ala657Thr in the GluK2 receptor subunit. We engineered this mutation in the mouse *Grik2* gene, yielding a GluK2(A657T) mouse, and studied mice of both sexes to determine how hippocampal neuronal function is disrupted. Synaptic KAR currents in hippocampal CA3 pyramidal neurons from heterozygous A657T mice exhibited slow decay kinetics, consistent with incorporation of the mutant subunit into functional receptors. Unexpectedly, CA3 neurons demonstrated elevated action potential spiking because of downregulation of the small-conductance Ca^{2+} activated K^+ channel (SK), which mediates the post-spike afterhyperpolarization. The reduction in SK activity resulted in increased CA3 dendritic excitability, increased EPSP-spike coupling, and lowered the threshold for the induction of LTP of the associational-commissural synapses in CA3 neurons. Pharmacological inhibition of SK channels in WT mice increased dendritic excitability and EPSP-spike coupling, mimicking the phenotype in A657T mice and suggesting a causative role for attenuated SK activity in aberrant excitability observed in the mutant mice. These findings demonstrate that a disease-associated missense mutation in *GRIK2* leads to altered signaling through neuronal KARs, pleiotropic effects on neuronal and dendritic excitability, and implicate these processes in neuropathology in patients with genetic NDDs.

Key words: dendritic excitability; hippocampus; kainate receptor; SK channels

Significance Statement

Damaging mutations in genes encoding synaptic proteins have been identified in various neurodevelopmental disorders, but the functional consequences at the cellular and circuit level remain elusive. By generating a novel knock-in mutant mouse, this study examined the role of a pathogenic mutation in the GluK2 kainate receptor (KAR) subunit, a subclass of ionotropic glutamate receptors. Analyses of hippocampal CA3 pyramidal neurons determined elevated action potential firing because of an increase in dendritic excitability. Increased dendritic excitability was attributable to reduced activity of a Ca^{2+} activated K^+ channel. These results indicate that a pathogenic KAR mutation results in dysregulation of dendritic K^+ channels, which leads to an increase in synaptic integration and backpropagation of action potentials into distal dendrites.

Received July 7, 2023; revised Sep. 12, 2023; accepted Sep. 16, 2023.

Author contributions: T.N., Y.-Z.W., J.N.S., G.T.S., and A.C. designed research; T.N., S.T., Y.-Z.W., N.-H.Y., A.P.W., C.C.M.C., K.M.F., J.X., and J.N.A. performed research; T.N., S.T., Y.-Z.W., N.-S.Y., C.C.M.C., J.X., J.N.A., J.N.S., and A.C. analyzed data; T.N. wrote the first draft of the paper; T.N., S.T., Y.-Z.W., N.-H.Y., A.P.W., C.C.M.C., K.M.F., J.X., J.N.A., J.N.S., G.T.S., and A.C. edited the paper; J.N.S., G.T.S., and A.C. wrote the paper.

This work was supported by National Institutes of Health/National Institute of Neurological Disorders and Stroke R01NS105502 to G.T.S. and A.C.; and National Institutes of Health/National Institute of Neurological Disorders and Stroke R01NS115471 to A.C. Mice were generated with the assistance of Northwestern University Transgenic and Targeted Mutagenesis Laboratory.

The authors declare no competing financial interests.

Correspondence should be addressed to Anis Contractor at a-contractor@northwestern.edu.

https://doi.org/10.1523/JNEUROSCI.1259-23.2023

Introduction

Rare *de novo* variants causative for neurodevelopmental disorders (NDDs) occur in a variety of genes that code for synaptic proteins, including ionotropic glutamate receptors (iGluRs) (Yuan et al., 2015). iGluRs are central to excitatory neurotransmission and critical for normal development of the brain. *De novo* pathogenic variants have been identified in genes that encode each of the four classes of iGluRs and gain- and loss-of-function variants cause disorders with a spectrum of clinical features that include intellectual disability and global developmental delay (Wu et al., 2007; Burnashev and Szepetowski, 2015; Lemke

et al., 2016; Davies et al., 2017; Geisheker et al., 2017; Guzman et al., 2017; Martin et al., 2017; Platzer et al., 2017; Myers et al., 2019; Salpietro et al., 2019; Stolz et al., 2021; Coombs et al., 2022). The number of damaging iGluR gene mutations identified in patients with NDDs continues to grow, but it remains to be determined how specific variants cause changes to brain development or function that result in cognitive, motor, and other phenotypes.

In the *GRIK2* kainate receptor (KAR) gene, damaging missense variants alter channel function, protein expression, and trafficking of assembled complexes to the plasma membrane (Guzman et al., 2017; Stolz et al., 2021). The first such variant, p.Ala657Thr, was discovered in a child whose primary clinical features were global developmental delay, intellectual disability, and an ataxic gait (Guzman et al., 2017). More recently, additional individuals with similar neurodevelopmental symptoms were discovered to have the same variant (Stolz et al., 2021). The *GRIK2* p.Ala657Thr variant occurs at a position in the GluK2 receptor protein critical to function that is part of a highly conserved set of residues, the SYTANLAAF motif, which form the distal segment of the M3 transmembrane pore-forming domain and affects gating of the receptor channel. An analogous mutation in the mouse *Grid2* iGluR gene was the first such reported *de novo* variant and is causative for an ataxic phenotype in the "Lurcher" strain of inbred mice. This mutation in *Grid2* results in a constitutively active GluD2 δ receptor that causes Purkinje neuron degeneration (Zuo et al., 1997; Vogel et al., 2007), and has also been identified in humans (Coutelier et al., 2015). Pathogenic variants at the analogous alanine in *GRIA* AMPAR genes result in NDDs that include autism spectrum disorder in some children (Davies et al., 2017; Geisheker et al., 2017; Martin et al., 2017; Coombs et al., 2022).

KARs are expressed across a wide range of brain regions in both excitatory and inhibitory neurons but in most are excluded from postsynaptic densities and therefore do not mediate fast, phasic synaptic depolarizations. Genetic and pharmacological studies implicate KARs in the fine-tuning of neurotransmitter release from presynaptic terminals (Contractor et al., 2001; Schmitz et al., 2001; Pinheiro et al., 2007). Other unconventional activities include promoting the functional expression of K^+-Cl^- cotransporter isoform 2 (KCC2) (Mahadevan et al., 2014) and actively suppressing the post-spike afterhyperpolarization (AHP), which elevates neuronal excitability (Cherubini et al., 1990; Melyan et al., 2002; Fisahn et al., 2005). KARs also modulate important synaptic properties, neuronal morphology, maturation, and plasticity during development (Lauri et al., 2021). While the mechanistic roles that KARs play in modulating circuit development are not yet fully known, and may be quite heterogeneous, in many cases these involve noncanonical, G protein-mediated signaling pathways distinct from ionotropic function of the receptor (Rodriguez-Moreno and Lerma, 1998; Melyan et al., 2002; Rozas et al., 2003) and tonic, nonphasic activation by ambient glutamate (Vesikansa et al., 2012). Therefore, damaging KAR gene variants have the potential to disrupt key aspects of neuronal signaling and development of the CNS, consistent with clinical phenotypes in children with *GRIK2* mutations (Guzman et al., 2017; Stolz et al., 2021).

In this study, we have examined the consequences of aberrant KAR signaling in a mouse line harboring the mutant *Grik2* allele that generates the p.Ala657Thr alteration, referred to as GluK2 (A657T) mice. Our examination was focused on determining how receptors containing the mutant subunit disrupt excitability and synaptic function in hippocampal CA3 pyramidal neurons, where the signaling properties of KARs have been extensively characterized (Castillo et al., 1997; Mulle et al., 1998; Contractor et al., 2000). Surprisingly, spontaneous action potential (AP) frequency was elevated in CA3 neurons. There was also a decrease in the AHP in CA3 neurons of GluK2(A657T) mice that correlated with enhanced dendritic excitability and increased EPSP coupling to APs of distal associational-commissural (AC) synapses. Elevated dendritic excitability also boosted the spread of backpropagating APs (bAPs), and AC synapses exhibited a reduced threshold for the induction on NMDA receptor (NMDAR)-dependent LTP. Altered dendritic excitability was because of an apparent functional downregulation of small-conductance Ca^{2+} activated K^+ channels (SK) in A657T mice. These results demonstrate that a *Grik2* mutation that models a human genetic NDD causes profound disruptions in hippocampal function that at least in part arise from processes that alter dendritic excitability.

Materials and Methods

Animal care and use. All experimental procedures were conducted in accordance with the ethical policies and protocols approved by the Northwestern University Institutional Animal Care and Use Committee. The point mutation was engineered into the genome of the mouse using the CRISPR/Cas9 gene editing system to generate the A657T amino acid substitution in the mouse *Grik2* gene. Single guide RNAs, Cas9 mRNA and a single strand oligonucleotide donor (ss donor) with a single base mutation were microinjected into mouse zygotes. Founders with the positively identified A657T mutation were bred with WT C57/bl6J mice, and each of these founders produced viable heterozygous mutant mice. Successful generation of the founders and offspring was confirmed by direct sequencing. Heterozygous mutant male mice were crossed with WT female mice for breeding, and both male and female WT and heterozygous A657T littermates were used for experiments. Mice were housed with food and water provided *ad libitum* under 12/12 h dark-light cycle. Experiments were conducted with the investigator blind to the genotype of the animals. These were subsequently confirmed by tail biopsy samples via *post hoc* sequencing and/or PCR.

Electrophysiology. Male and female GluK2 WT or A657T heterozygous mice (3-5 weeks old) were deeply anesthetized with inhalation of isoflurane and an intraperitoneal injection of xylazine (10 mg/kg) and ketamine (100 mg/kg). Mice underwent trans-cardiac perfusion with an ice-cold sucrose ACSF solution containing the following (in mM): 85 NaCl, 2.5 KCl, 1.25 NaH_2PO_4, 25 $NaHCO_3$, 25 glucose, 75 sucrose, 0.5 $CaCl_2$, and 4 $MgCl_2$, including 10 μM DL-APV and 100 μM kynurenate. Horizontal brain sections (350 µm thick) were prepared in the same ice-cold sucrose ACSF on a Leica Vibratome (Leica Microsystems). Slices were incubated in sucrose ACSF at 30°C-32°C for ~30 min; then the solution was gradually exchanged for a recovery ACSF containing the following (in mM): 125 NaCl, 2.4 KCl, 1.2 NaH_2PO_4, 25 $NaHCO_3$, 25 glucose, 1 $CaCl_2$, and 2 $MgCl_2$, including 10 μM DL-APV and 100 μM kynurenate at room temperature (RT). Slices were transferred to a recording chamber after a recovery period of at least 1.5 h and were visualized under Dodt-Gradient-Contrast optics (Luigs & Neumann). During recordings, slices were perfused with normal ACSF (28°C-30°C) containing the following (in mM): 125 NaCl, 2.4 KCl, 1.2 NaH_2PO_4, 25 $NaHCO_3$, 25 glucose, 2 $CaCl_2$, and 1 $MgCl_2$ continuously equilibrated with 95% O_2 and 5% CO_2. Standard techniques were used to make patch-clamp recordings from visually identified CA3 pyramidal neurons in the hippocampus. Recording electrodes had tip resistances of 2-4 MΩ when filled with a cesium-based internal solution containing the following (in mM): 95 CsF, 25 CsCl, 10 Cs-HEPES, 10 Cs-EGTA, 2 NaCl, 2 Mg-ATP, 10 QX-314, 5 tetraethylammonium (TEA)-Cl, and 5 4-AP for voltage-clamp recordings or a potassium-based internal solution containing the following (in mM): 125 $KMeSO_4$, 5 KCl, 5 NaCl, 0.02 EGTA, 11 HEPES, 1 $MgCl_2$, 10 phosphocreatine, 4 Mg-ATP, 0.3 Na-GTP for current-clamp recordings unless further specified. Liquid junction potential was not corrected. In voltage-clamp, access resistance (R_a)

was continuously monitored, and recordings were discarded when R_a showed >20% change during the experiments. For voltage-clamp recordings, cells were held at −70 mV unless otherwise specified. Data were acquired and analyzed using a Multiclamp 700B amplifier and pClamp 10 software (Molecular Devices).

Synaptic afferents were stimulated with a monopolar glass electrode filled with normal ACSF positioned in the *stratum lucidum* or in the *stratum radiatum* to elicit mossy fiber (MF) or AC-mediated synaptic responses. EPSCs were isolated using the $GABA_A$ receptor antagonists bicuculline (10 μM) and picrotoxin (50 μM). MF-EPSCs were characterized by large short-term synaptic plasticity, rapid rise-time kinetics, and when appropriate the Group II mGluR agonist DCG-IV was applied at the end of recordings (Armstrong et al., 2006; Fernandes et al., 2009). Kainate receptor-mediated EPSCs ($EPSC_{KAR}$) were isolated using the AMPAR antagonist GYKI-53655 (50 μM). EPSC decay kinetics were quantified by fitting the traces with single or double exponential. For MF-LTP recordings, repeated tetanic stimuli composed of 100 bursts at 100 Hz repeated 3 times every 20 s were applied after obtaining a 10 min stable baseline. IPSCs were recorded in the presence of AMPA and kainate receptor blockers CNQX (10 μM) and an NMDAR blocker D-APV (50 μM).

For AC-LTP experiments, field EPSPs (fEPSPs) were measured using extracellular recordings. Recording electrodes had tip resistances of 2-4 MΩ when filled with normal ACSF. Stimulating and recording electrodes were placed in the stratum radiatum. The slope of the fEPSPs was measured for LTP recordings. After obtaining a stable baseline for at least 10 min, picrotoxin was perfused into the recording solution for 5 min to block $GABA_A$ receptors. Short-burst high-frequency stimuli (4 bursts at 50 Hz repeated 10 times every second) was applied to induce LTP of AC-fEPSPs (Kobayashi and Poo, 2004).

Spontaneous AP firing was measured in cell-attached recordings of action currents in voltage-clamp mode. For cell-attached experiments, the recording electrodes had tip resistances of 3-5 MΩ when filled with the same potassium-based internal solution as for current-clamp recordings. The effect of NBQX on firing frequency was analyzed by a paired comparison in each cell between baseline and NBQX-treated conditions.

Intrinsic cellular properties were analyzed in current-clamp recordings as previously described (Nomura et al., 2017). Resting membrane potential was determined by switching the recording mode to current clamp immediately after forming the whole-cell configuration. Rheobase was measured by gradually increasing the size of injected depolarizing square currents in 5 pA increments until the first AP was elicited. AP threshold was considered to be the potential where the first derivative of the AP (*dV/dt*) showed an abrupt upward inflection when *dV/dt* was plotted against the corresponding membrane voltage. Input–output (I-O) frequency response curves for APs were generated by injecting depolarizing square currents (0-1000 pA with 100 pA increments, 500 ms width) to analyze AP firing properties. Baseline membrane voltage was adjusted to −65 mV by injecting continuous currents through the patch pipettes.

Voltage-dependent conductances were analyzed in voltage-clamp recordings using a K^+-based internal solution. For recordings of total Na^+ (INa^+_{total}) and K^+ (IK^+_{total}) conductances, membrane potential was clamped, and depolarizing step currents (500 ms) were injected from −70 to 30 mV (5 mV increments). INa^+_{total} could be detected starting at ~−50 to −40 mV in most cells. IK^+_{total} was measured by averaging the plateau current of the last 5 ms during the voltage steps. Voltage-dependent fast K^+ current (A-current; I_A) was measured in normal ACSF, but concentrations of Ca^{2+} and Mg^{2+} were modified to 0 and 3 mM, respectively, to block Ca^{2+} mediated and activated currents. The Na^+ channel blocker TTX (0.5 μM) and the K^+ channel blocker TEA (1 mM) were included in the recording solution to block Na^+ currents and TEA-sensitive K^+ currents. Cells were clamped at −80 mV and depolarized to 20 mV with a depolarizing voltage step (200 ms) followed by an identical voltage step 100 ms after the first step to activate voltage-dependent K^+ channels. I_A was measured as the percentage of the peak current evoked by the second voltage step relative to the current evoked by the first step, reflecting fast recovery of the channels from inactivation (Chen et al., 2006).

EPSP-AP coupling was analyzed using stimulation of EPSP that was termed minimal using the following experimental criteria. After obtaining a recording of an EPSP stimulation, intensity was reduced to the minimum at which it was possible to evoke a synaptic response with no observed failures. This resulted in starting EPSPs that were not different between genotypes for either MF or AC EPSPs. Baseline membrane voltage was adjusted to −65 mV by injecting continuous currents through the recording electrodes. Spike probability in each stimulation bin was measured in ~10 sweeps and was then averaged in each cell.

AHPs and I_{AHP} were induced by depolarizing currents injection in current-clamp and voltage-clamp recordings, respectively. In current-clamp recordings, the baseline voltage was maintained at −65 mV with continuous current injection. Depolarizing square current injection (0-1000 pA with 100 pA increments, 500 ms width) was used to induce AHPs. Medium AHP (mAHP) and slow AHP (sAHP) were measured at their peaks typically several tens of milliseconds (mAHP) and several hundreds of milliseconds (sAHP) after the depolarizing step. When the peaks were not clearly distinguishable, mAHP and sAHP were measured at 50-100 ms (mAHP) and 500-1000 ms (sAHP) after the depolarization. In voltage-clamp recordings, I_{mAHP} and I_{sAHP} were evoked by depolarizing the cells from −60 to 60 mV with square pulses (pulse width: 40, 80, 160, and 320 ms) and peaks measured typically at several tens of milliseconds for I_{mAHP} and several hundreds of milliseconds for I_{sAHP} after the depolarization. When the peak currents were not clearly delineated the, I_{mAHP} and I_{sAHP} were measured 20-100 ms (I_{mAHP}) and 150-1150 ms (I_{sAHP}) after the depolarization.

Ca^{2+} imaging. Two-photon laser scanning microscopy (2PLSM) images of CA3 pyramidal neurons in the hippocampus were obtained using methods similar to those previously described (Day et al., 2008; Plotkin et al., 2013; Nomura et al., 2017). Cells were loaded with AlexaFluor-568 (50 μM) through the patch pipette for visualization. The dye was perfused intracellularly for at least 20 min after forming the whole-cell configuration. Images were acquired using a femtosecond pulsed excitation at 790 nm (Mira 900P with a Verdi 10W pump, Coherent Laser). Laser power was controlled with an M350 (KD*P) series Pockels cells (ConOptics). A Prairie Ultima (Bruker Nano, Fluorescence Microscopy Unit) scan head on an Olympus BX-61 upright microscope was used for imaging the slice with two Hamamatsu R3982 side on photomultiplier tubes. For Ca^{2+} imaging, cells were filled with the Ca^{2+} indicator Fluo-4 (200 μM) loaded through patch pipettes. Dendritic Ca^{2+} signals were triggered by 10 bAPs evoked by somatic suprathreshold depolarizing current injection (1 nA for 1 ms at 100 Hz). Ca^{2+} signals in multiple (typically 8-10) ROIs within a single branch of dendrites were acquired as fluorescent line scan signals in 3-5 pixels (0.77 μm) per line with 22.8 μs dwell time. The decay of the Ca^{2+} signals along the dendrite was fit using an exponential equation ($y = Ae^{-\lambda x}$) to derive the distance constant (λ) as a proxy of dendritic excitability. All components were configured and acquired using Multiclamp 700B amplifier and Prairie View 9.0 software (Bruker).

Wheel running. A wireless low profile running wheel (Med Associates) was placed into the homecage of single housed mice during the dark cycle. Mice were allowed free access to the wheel for 90-120 min and running activity logged for each animal. Mice were killed and brain removed for cFos immunohistochemistry.

Immunohistochemistry. Immunohistochemistry for GluK2/3 was conducted according to prior published methods (Barthet et al., 2022). Briefly, mice were anesthetized with isoflurane, decapitated, brains removed and rapidly frozen in liquid nitrogen or dry ice. Brains were sectioned coronally on a cryostat (50 μm), fixed in modified Carnoy's solution (1:6, acetic acid:ethanol), washed in PBS, permeabilized in 0.1% Triton X-100 and 0.05% Tween 20, blocked in 5% newborn calf serum with 0.05% Tween 20, and incubated overnight at 4°C in rabbit anti-GluK2/3, (1:100; Invitrogen PA1-37 780) and mouse anti-NeuN, (1:250; Millipore MAB377). The following day, the sections were washed in PBS and incubated with goat anti-rabbit-488 and goat anti-mouse-568 (1:200) for 2 h, washed with PBS, and coverslipped with ProLong Diamond mounting media containing DAPI (Fisher Scientific).

Immunohistochemistry for cFos was conducted according to the general method described previously (Armstrong et al., 2006). Briefly, mice were anesthetized with isoflurane and perfused through the heart with PBS containing 0.02% sodium nitrite, followed by 2% PFA in 0.1 M sodium acetate buffer, pH 6.5, and 2% PFA in 0.1 M sodium borate

buffer, pH 8.5. The brains were removed from the skull, postfixed for 3 h, and sectioned on a vibrating microtome (Leica Vibratome, VT1000). Free-floating, coronal sections (50 μm) were washed in TBS containing 0.01% H_2O_2, permeabilized in TBS containing 0.001% Triton X-100 and 0.001% NP40, and blocked for 1 h in TBS containing 0.05% BSA (TBS-BSA), 1% normal donkey serum, and unconjugated donkey anti-rabbit IgG (1:1000). Sections were then washed in TBS-BSA and incubated overnight on a shaker in TBS-BSA containing rabbit anti-cFos (1:2000; Cell Signaling Product #2250). The following day, the sections were washed in TBS-BSA and incubated in TBS-BSA, 0.25% normal donkey serum and donkey anti-rabbit IgG-biotin (1:1000) for 1 h. The sections were then washed in TBS and incubated for 1 h in TBS containing streptavidin-biotin-peroxidase complex (ABC 1:1000 TBS; Fisher Scientific, Product #32020), washed again in TBS, and incubated in TBS containing diaminobenzidine. Sections were mounted onto slides, air-dried overnight, dehydrated in ethanol, xylene, and coverslipped using Permount.

Synaptosome preparation and protein gels. P3 synaptosomes containing the large MF fraction were prepared as previously described (Armstrong et al., 2006). Briefly, hippocampi isolated from adult mice were homogenized in 0.325 M sucrose and then centrifuged at 900 × *g* for 10 min at 4°C. The supernatant containing the small synaptosomes (P2) was collected, and the remainder resuspended in 0.325 M sucrose and centrifuged at 900 × *g* for an additional 10 min at 4°C. The pooled supernatants were then centrifuged at 17,000 × *g* for 55 min at 4°C. The resultant pellet is enriched with small hippocampal synaptosomes (P2). The large MF synaptosomes sedimented with the nuclei after the initial low-speed spin and were resuspended in 1.5 ml of 18% Ficoll in 0.325 M sucrose and centrifuged at 7500 × *g* for 40 min. The supernatant from this spin was collected, diluted in 4 volumes 0.3 M sucrose, and centrifuged at 13,000 × *g* for 20 min at 4°C to yield the P3 pellet containing the large MF synaptosomes.

Protein isolated from the small hippocampal synaptosomes (P2) and the large MF synaptosomes (P3) was diluted in 0.325 M sucrose and loading buffer (50 mM Tris-Cl, 100 mM β-mercaptoethanol, 2% SDS, 0.1% bromophenol blue, and 10% glycerol) and run on a 4%-12% gradient polyacrylamide gel. Gels were transferred to PVDF membrane, blocked in 20 mM TBS containing 3% IgG-free BSA and 1% normal donkey serum, and blotted overnight in the same solution containing the following antibodies: mouse anti-β-actin (1:30,000), rabbit anti-GluK2/3 (1:1000), and mouse anti-postsynaptic density 95 (PSD95) (1:5000). The following day, blots were washed 3 × 5 min in TBS and incubated for 1 h in the blocking solution (above) containing both secondary antibodies (donkey anti-rabbit IgG, donkey anti-mouse IgG) and visualized on a Li-Cor Odyssey Fc fluorescent imager.

Sample preparation for mass spectrometry (MS). Tissue from the CA3 region of the hippocampus was micro-dissected from WT and A657T Het mice and homogenized in RIPA lysis buffer (50 mM Tris base, 150 mM NaCl, 1% Triton X-100, 2 mM EDTA, 1% sodium deoxycholate, and 1% SDS with complete Mini, EDTA-free protease inhibitor cocktail) using the Kimble Pellet Pestle cordless motor and grinders. Homogenates were rotated at 4°C for 30 min and pelleted by centrifugation for 15 min at 14,000 × *g*. The supernatant was separated into a new tube, precipitated using the chloroform/methanol method, denatured with 8 M urea (in a 100 mM ammonium bicarbonate [ABC] vortex 1 h at RT), and processed with ProteaseMAX according to the manufacturer's protocol. The samples were reduced with 5 mM Tris(2-carboxyethyl) phosphine (vortexed for 1 h at RT), alkylated in the dark with 10 mM iodoacetamide (20 min at RT), diluted with 100 mM ABC, and quenched with 25 mM Tris(2-carboxyethyl)phosphine. Samples were sequentially digested with Lys-C (2 h at 37°C with shaking) and trypsin (overnight at 37°C with shaking), acidified with trifluoroacetic acid (TFA) to a final concentration of 0.1%, and spun down (15,000 × *g* for 15 min at RT) wherein the supernatant was moved to a new tube. The samples were desalted using Peptide Desalting Spin Columns (89852; Pierce) and dried down with vacuum centrifugation. The samples were resuspended in 100 mM HEPES, pH 8.5. Micro BCA (23235, Pierce) assay was performed to determine the peptide concentration, and 95 μg of each sample was used for isobaric labeling. Tandem Mass Tags (TMT) labeling was performed on the samples according to the manufacturer's instructions (A44520; Fisher Scientific). After incubation for 2 h at RT, the reaction was quenched with 0.3% (v/v) hydroxylamine, isobaric-labeled samples were combined 1:1:1:1:1:1:1:1:1:1, and the pooled sample was dried down with vacuum centrifugation. The sample was resuspended in 0.1% TFA solution, desalted using Peptide Desalting Spin Columns (89852; Pierce), and dried down with vacuum centrifugation. The sample was resuspended in 0.1% TFA solution and fractionated into eight fractions using a High pH Reversed-Phase Peptide Fractionation Kit (84868; Pierce) wherein fractions were step eluted in 300 μl of buffer of increasing acetonitrile concentrations with decreasing concentrations of 0.1% triethylamine per the manufacturer's instructions (5.0%, 10.0%, 12.5%, 15.0%, 17.5%, 20.0%, 22.5%, 25.0%, and 50% of ACN in 0.1% triethylamine solution). The fractions were dried down with vacuum centrifugation. The high pH peptide fractions were directly loaded into the autosampler for MS analysis without further desalting.

Mass spectrometry. Two micrograms of each fraction or sample were auto-sampler loaded with an UltiMate 3000 HPLC pump onto a vented Acclaim Pepmap 100, 75 μm × 2 cm, nanoViper trap column coupled to a nanoViper analytical column (Fisher Scientific, catalog #164570, 3 μm, 100 Å, C18, 0.075 mm, 500 mm) with stainless-steel emitter tip assembled on the Nanospray Flex Ion Source with a spray voltage of 2000 V. An Orbitrap Fusion (Fisher Scientific) was used to acquire all the MS spectral data. Buffer A contained 94.785% H_2O with 5% ACN and 0.125% FA, and Buffer B contained 99.875% ACN with 0.125% FA. For TMT MS experiments, the chromatographic run was for 4 h in total with the following profile: 0%-7% for 7, 10% for 6, 25% for 160, 33% for 40, 50% for 7, 95% for 5, and again 95% for 15 min, respectively.

We used a multiNotch MS3-based TMT method to analyze all the TMT samples (Ting et al., 2011; McAlister et al., 2014). The scan sequence began with an MS1 spectrum (Orbitrap analysis, resolution 120,000, 400-1400 Th, AGC target 2×10^5, maximum injection time 200 ms). MS2 analysis, Top speed (2 s), Collision-induced dissociation (CID, quadrupole ion trap analysis, AGC 4×10^3, NCE 35, maximum injection time 150 ms). MS3 analysis, top 10 precursors, fragmented by HCD before Orbitrap analysis (NCE 55, max AGC 5×10^4, maximum injection time 250 ms, isolation specificity 0.5 Th, resolution 60,000).

MS data analysis and quantification. Protein identification/quantification and analysis were performed with Integrated Proteomics Pipeline-IP2 (Bruker) using ProLuCID (Eng et al., 1994; Xu et al., 2015), DTASelect2 (Tabb et al., 2002; Cociorva et al., 2007), and Census and Quantitative Analysis (for TMT MS experiments). Spectrum raw files were extracted into MS1, MS2, and MS3 (for TMT experiments) files using RawConverter (http://fields.scripps.edu/downloads.php). The tandem mass spectra were searched against UniProt mouse protein database (downloaded on October 26, 2020) (UniProt Consortium, 2015) and matched to sequences using the ProLuCID/SEQUEST algorithm (ProLuCID, version 3.1) with 5 ppm peptide mass tolerance for precursor ions and 600 ppm for fragment ions. The search space included all fully and half-tryptic peptide candidates within the mass tolerance window with no-miscleavage constraint, assembled, and filtered with DTASelect2 through IP2. To estimate peptide probabilities and false discovery rates (FDRs) accurately, we used a target/decoy database containing the reversed sequences of all the proteins appended to the target database (Peng et al., 2003). Each protein identified was required to have a minimum of one peptide of minimal length of six amino acid residues; however, this peptide had to be an excellent match with an FDR $<1\%$ and at least one excellent peptide match. After the peptide/spectrum matches were filtered, we estimated that the peptide FDRs were $\leq 1\%$ for each sample analysis. Resulting protein lists include subset proteins to allow for consideration of all possible protein forms implicated by at least three given peptides identified from the complex protein mixtures. Then, we used Census and Quantitative Analysis in IP2 for protein quantification of the TMT MS experiment. TMT MS data were normalized using the built-in method in IP2.

Spyder (MIT, Python 3.7, libraries, "numpy," "scipy") was used for data analyses. RStudio (version, 1.2.1335, packages, "tidyverse") was used for data virtualization. The Database for Annotation, Visualization and Integrated Discovery (https://david.ncifcrf.gov/) was used for protein functional annotation analysis.

Quantification and statistical analysis. Statistical analyses were done using GraphPad Prism (GraphPad Software), and Origin (OriginLab) software. Comparisons were made using Mann–Whitney *U* test or the Kolmogorov–Smirnov test for unpaired two samples. Paired two samples were compared using Wilcoxon signed-rank test. For multiple comparisons, repeated two-way ANOVA followed by *post hoc* Bonferroni's correction was used. Differences were considered to be significant when $p < 0.05$. Data are presented as mean ± SEM.

Results

Synaptic KARs are modified in GluK2(A657T) mice

To understand how the Ala657Thr mutation affects brain function, we engineered a mouse with a single amino acid swap from alanine (A) to threonine (T) in the GluK2 receptor subunit using CRISPR editing. Heterozygous GluK2(A657T) mice were viable, but no living homozygous mice were observed, suggesting that a biallelic Ala657Thr mutation in *Grik2* is embryonic lethal. In hippocampal sections, GluK2/3 immunoreactivity appeared similar to that in WT mice in the dentate gyrus (DG) and CA3 regions where KARs are abundantly localized (Fig. 1*A*). Western blot analysis of the P2 and P3 fractions (enriched for large MF boutons) (Armstrong et al., 2006) from hippocampal extracts demonstrated that there were no major disruptions in synaptic expression of GluK2/3 protein (P2 fraction: $n = 3$, $p = 0.24$; P3 fraction: $n = 3$, $p = 0.54$; *t* test) (Fig. 1*B*,*C*). As a discovery-based screen of potential differentially expressed proteins in GluK2 (A657T) mice, we used TMT-based quantitative MS analysis to compare the CA3 proteomes in WT and A657T heterozygous mice (Fig. 1*D*,*E*). We found that protein levels were highly similar between the two genotypes; indeed, only ~0.89% of CA3 proteins were significantly altered in the A657T bulk CA3 extracts (for full dataset, see Extended Data Table 1-1). Bioinformatic Gene Ontology enrichment analysis of the significantly elevated or reduced proteins revealed no significantly enriched terms. Importantly, NMDAR and AMPAR proteins were not different in WT and A657T mice. These data demonstrate that introduction of the *Grik2* p.Ala657Thr allele has only a minor effect on the CA3 proteome and that synaptic proteins are expressed at similar levels as in the WT littermates.

To test whether the mutant subunit assembled into functional synaptic KARs, we recorded $EPSC_{KAR}$ from CA3 pyramidal neurons, which localize postsynaptic GluK2-containing receptors exclusively to MF synapses (Castillo et al., 1997; Mulle et al., 1998). Voltage-clamp recordings were made from CA3 pyramidal neurons, and MF inputs were electrically stimulated in the stratum lucidum. AMPARs were inhibited with GYKI-53655 (50 μM), leaving the isolated $EPSC_{KAR}$ (Fig. 1*F*,*G*). The relative amplitude of $EPSC_{KAR}$ normalized to the total $EPSC_{AMPAR/KAR}$ was not different between WT and A657T mice, consistent with normal expression of GluK2-containing KARs in the mutant mice (WT: 6.8 ± 1.2%, $n = 5$ cells, 3 mice; A657T: 6.7 ± 0.9%, $n = 8$ cells, 5 mice; $p = 1.0$; Mann–Whitney) (Fig. 1*H*). As predicted (Guzman et al., 2017), the decay kinetics of $EPSC_{KAR}$ were significantly slower in recordings from the A657T mice, demonstrating that mutant subunits are incorporated into synaptic KARs (WT: 37.0 ± 4.1 ms, $n = 5$ cells, 3 mice; A657T: 138.7 ± 18.9 ms, $n = 8$ cells, 5 mice; $p = 0.0016$; Mann–Whitney) (Fig. 1*I*). Prior recordings of mutant GluK2A657T receptors in recombinant systems have demonstrated a constitutive steady-state current in the nominal absence of agonist (Guzman et al., 2017). To determine whether we could detect a standing current in CA3 neurons in A657T mice, we measured the change in holding current after application of the nonspecific AMPA/KAR antagonist NBQX (50 μM). We found that, in recordings from CA3 neurons in WT mice, there was no change in holding current after NBQX (WT: 2.74 ± 3.10 pA, $n = 22$ cells, 7 mice), whereas there was a small current detected in A657T recordings (A657T: 16.6 ± 3.58 pA, $n = 16$ cells, 4 mice; $p = 0.0012$, Mann–Whitney) (Fig. 1*J*,*K*). Thus, neuronal KARs containing the mutant GluK2 subunit exhibited at least some of the altered functional properties predicted by studies of recombinant receptors.

Analyses of KAR-mediated currents uncovered an aberrant ionotropic KAR function in GluK2(A657T) mice. We therefore assessed whether parameters of MF synaptic physiology known to be disrupted in GluK2 null mice (Contractor et al., 2001) were altered in the A657T mice. Unexpectedly, there were no changes apparent in paired-pulse facilitation (Fig. 2*A*,*B*), short-term plasticity during trains of stimuli at 1 Hz (Fig. 2*C*,*D*), or NMDAR-independent MF LTP compared with WT mice (Fig. 2*E*,*F*). These results demonstrate that mutant GluK2(A657T) subunits readily incorporate into neuronal KARs, slow deactivation kinetics of the $EPSC_{KAR}$, and underlie a tonic current in CA3 neuron recordings in the slice; however, they do not affect expression of synaptic receptors or their influence on presynaptic forms of potentiation at MF synapses.

CA3 pyramidal neurons are more excitable in A657T mice

To further test whether the A657T mutation affects the functional properties of neurons in the CA3 region, we first recorded spontaneous AP firing (action currents) in CA3 neurons. The majority of neurons in WT mice were silent throughout the recording period (5 min), with only 40% (17 of 42) of cells firing at least one AP. In contrast, 84% (27 of 32) of CA3 pyramidal neurons in A657T mice were spontaneously active, and the average spike frequency was higher than that in neurons from WT mice (WT: 0.19 ± 0.11 Hz, $n = 42$ cells, 17 mice; A657T: 0.38 ± 0.21 Hz, $n = 32$ cells, 8 mice; $p = 0.000012$; Kolmogorov–Smirnov) (Fig. 3*A*,*B*).

Spontaneous AP firing is dependent on both the intrinsic properties of pyramidal neurons as well as integration of inhibitory and excitatory synaptic input (Cohen and Miles, 2000), either of which could be affected in CA3 neurons in A657T mice. We assessed these parameters in recordings of synaptic currents and intrinsic properties of CA3 neurons. We determined that the resting membrane potential was more depolarized (WT: −68.0 ± 1.7 mV, $n = 27$ cells, 8 mice; A657T: −61.2 ± 1.5 mV, $n = 24$ cells, 7 mice; $p = 0.0069$; Mann–Whitney) and the input resistance (R_{in}) was lower (WT: 207.3 ± 10.9 MΩ, $n = 28$ cells, 14 mice; A657T: 168.7 ± 8.1 MΩ, $n = 44$ cells, 18 mice; $p = 0.0035$; Mann–Whitney) in CA3 pyramidal neurons from A657T mice compared with WT, which could be attributed in part to the standing KAR current we had measured in CA3 neurons. In contrast, there were no significant differences in rheobase (WT: 161.56 ± 26.7 pA, $n = 16$ cells, 6 mice; A657T: 166 ± 16.2 pA, $n = 15$ cells, 6 mice, $p = 0.49$; Mann–Whitney) or AP threshold (WT: −39.4 ± 2.0 mV, $n = 16$ cells, 6 mice; A657T: −43.1 ± 1.3 mV, $n = 15$ cells, 6 mice, $p = 0.32$; Mann–Whitney) in A657T mice. When APs were evoked by somatic depolarization, the I-O AP curve was indistinguishable between WT and A657T mice (WT: $n = 16$ cells, 6 mice; A657T: $n = 13$ cells, 5 mice; two-way ANOVA, $F_{(1,27)} = 0.0003$, $p = 0.99$) (Fig. 3*I*,*J*). We also found that voltage-dependent conductances that contribute to the AP firing, including the total K^+ current (IK^+_{total}) and the total Na^+ (INa^+_{total}), were not different in CA3 neurons of A657T mice (not shown). Together, we interpreted these data as evidence that intrinsic properties likely play a

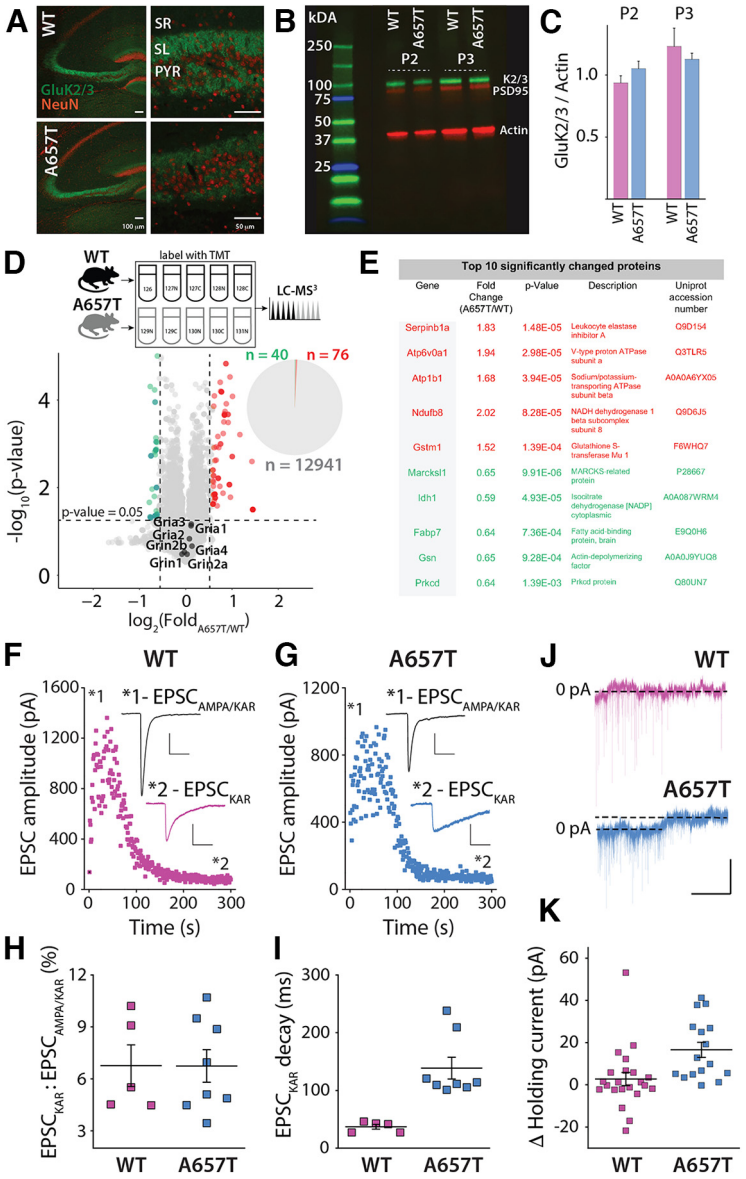

Figure 1. Aberrant kainate receptor-mediated currents and CA3 proteome in A657T mice. ***A***, Immunohistochemical analysis of KAR expression in the hippocampus. GluK2/3 labeling in the CA3 region was abundant in the termination zones of the MF axons in the stratum lucidum (SL) in both WT and A657T mice. SR, Stratum radiatum; PYR, pyramidal cell layer of CA3. Scale bars: left panels, 100 μm; right panels, 50 μm. ***B***, Representative Western blot of GluK2/3, PSD95, and actin in the P2 and P3 fractions from hippocampus of WT and A657T regions. ***C***, Quantification of Western blots. ***D***, Top, Experimental design to compare WT and A657T CA3 proteomes. Bottom, Volcano plot represents comparison of relative protein abundance in WT and A657T mutant CA3. The major NMDAR and AMPAR protein subunit isoforms are indicated on the plot. Pie chart represents that only ~0.89% CA3 proteins are differentially expressed in A657T CA3. $n = 5$ mice per genotype. Significance was assessed using Student's t test. ***E***, Table of top 10 significantly differentially expressed proteins (red represents upregulated; green represents downregulated). Full dataset is available in Extended Data Table 1-1. ***F***, MF EPSCs recorded in CA3 neurons stimulating at 1 Hz to elevate release and measuring EPSCs before and after the application of AMPAR-selective antagonist GYKI-53655 (50 μM) in WT and (***G***) A657T mice. Inset, $EPSC_{AMPA/KAR}$ prior to antagonist and the residual $EPSC_{KAR}$ (magnified) after AMPAR blockade. Calibration: $EPSC_{AMPA/KAR}$, 250 pA, 50 ms; $EPSC_{KAR}$, 50 pA, 50 ms. ***H***, Analysis of EPSC amplitudes normalized to the amplitude of the total MF EPSCs. ***I***, Analysis of the decay of the $EPSC_{KAR}$. ***J***, Example traces of voltage-clamp recordings from CA3 neurons during application of NBQX (50 μM). Calibration: 50 pA, 60 s. ***K***, Change in holding current of CA3 neurons after NBQX in WT and A657T mice.

relatively minor role in the elevated AP firing observed in CA3 neurons in A657T mice.

We next tested whether synaptic excitation and inhibition are altered by measuring spontaneous postsynaptic currents (sEPSCs and sIPSCs). The frequency of sEPSCs was significantly elevated in A657T mice (WT: 1.9 ± 0.6 Hz, $n = 14$ cells, 6 mice; A657T: 4.4 ± 0.9 Hz, $n = 16$ cells, 5 mice; $p = 0.020$; Mann–Whitney) without a change in sEPSC amplitude ($p = 0.93$; Mann–Whitney) (Fig. 3*C–E*). Elevated sEPSC frequency, but not amplitude, is consistent with exaggerated AP firing and unaltered AMPAR protein level in A657T mice. In contrast, neither the frequency nor the amplitude of sIPSCs was different between CA3 pyramidal neurons in slices from WT and A657T mice (data not shown). Elevated AP spiking of CA3 therefore alters the balance of synaptic excitation to synaptic inhibition in these neurons.

Altered integration of synaptic input could generate the elevated AP frequency observed in our initial experiments. To test this possibility, we recorded spontaneous action currents while blocking EPSCs with the AMPA/kainate receptor antagonist NBQX (50 μM). Spontaneous spike firing in CA3 neurons from A657T mice was almost entirely eliminated by inhibition of

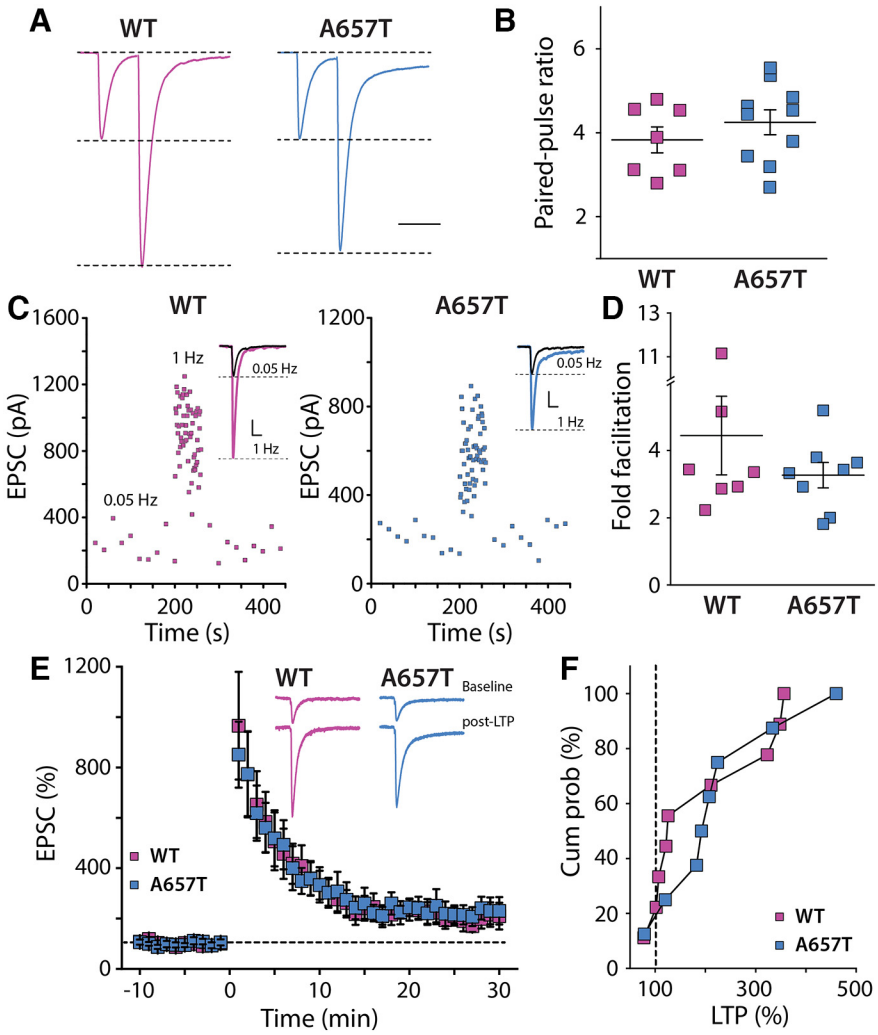

Figure 2. Presynaptic MF synaptic plasticity is not affected in A657T mice. ***A***, Example traces of pairs of MF EPSCs stimulated at an interstimulus interval of 40 ms to measure the paired-pulse ratio. ***B***, Grouped data of paired-pulse ratio of MF-CA3 EPSCs were not different between the genotypes (WT: 2.42 ± 0.15, $n = 7$ cells, 3 mice; A657T: 2.62 ± 0.15, $n = 10$ cells, 4 mice; $p = 0.36$; Mann-Whitney). ***C***, Example frequency facilitation experiment measuring MF EPSC amplitudes while elevating stimulation frequency from 0.05 to 1 Hz. Inset, Raw traces for each experiment in WT and A657T mice. ***D***, Grouped data for all experiments showing fold facilitation at 1 Hz, which was not different between genotypes (WT: 4.45 ± 1.17, $n = 7$ cells, 3 mice; A657T: 3.27 ± 0.38, $n = 8$ cells, 5 mice; $p = 0.78$; Mann-Whitney). ***E***, Time course for MF LTP induced by repeated tetanic stimulation (1 Hz for 1 s). Inset, Traces from one experiment of EPSCs during baseline recording and 25-30 min after induction of LTP. ***F***, Grouped data from all experiments represented as the cumulative % LTP. There was no difference in absolute LTP between genotypes (WT: 197.0 ± 38.4%, $n = 9$ cells, 8 mice; A657T: 224.8 ± 42.9%, $n = 8$ cells, 7 mice; $p = 0.78$; Mann-Whitney).

excitatory synaptic transmission with NBQX (Fig. 3*F*,*H*) with little apparent effect in WT mice (Fig. 3*G*). These data suggest that increased excitatory synaptic activity might contribute to spiking of CA3 neurons and increase recurrent network excitability in A657T mice.

We next sought to determine whether hippocampal neuronal spiking might be elevated *in vivo* in A657T mice. We assessed the expression of the immediate early gene cFos as a proxy for neuronal activity. Acute bouts of voluntary wheel running are known to elevate cFos expression in all hippocampal subregions (Oladehin and Waters, 2001; Chatzi et al., 2019; Tsuchida et al., 2022). We therefore tested whether cFos labeling is differentially elevated in mutant mice in CA3 pyramidal neurons and their upstream partners in the DG after a single exposure to a running wheel in their homecage (Fig. 4*A*). Mice in the A657T and WT groups did not demonstrate any differences in the total average running distance (WT: 0.809 ± 0.166 km, $n = 13$ mice; A657T: 0.768 ± 0.211 km, $n = 6$ mice, $p = 0.77$, Mann–Whitney) (Fig. 4*C*). We analyzed cFos-labeled cell density in the DG upper blade (DG_{UB}) and DG lower blade (DG_{LB}) and in regions CA3a-c (Fig. 4*A*,*B*, *D*, *E*). In each of these subregions, the density of cFos labeled neurons was elevated in A657T mice (DG_{UB}: $0.86 \pm 0.15 \times 10^{-3}/\mu m^2$, $1.86 \pm 0.33 \times 10^{-3}/\mu m^2$, $p = 0.030$; DG_{LB}: $0.63 \pm 0.14 \times 10^{-3}/\mu m^2$, $1.47 \pm 0.35 \times 10^{-3}/\mu m^2$, $p = 0.026$; CA3c: $1.20 \pm 0.24 \times 10^{-3}/\mu m^2$, $2.73 \pm 0.65 \times 10^{-3}/\mu m^2$, $p = 0.046$; CA3b: $1.24 \pm 0.20 \times 10^{-3}/\mu m^2$, $3.13 \pm 0.68 \times 10^{-3}/\mu m^2$, $p = 0.012$; CA3a: $0.90 \pm 0.20 \times 10^{-3}/\mu m^2$, $3.26 \pm 0.79 \times 10^{-3}/\mu m^2$, $p = 0.0047$; WT: $n = 13$ mice, A657T: $n = 6$ mice, Mann–Whitney) (Fig. 4*B*). Correlating the total density of cFos labeled neuron in the DG or CA3 with the total running distance also demonstrated a strong correlation between distance run by each mouse and density of cFos in each of these regions (Pearson's *r*: DG, WT: 0.64 DG, A657T: 0.60; CA3, WT: 0.70; CA3, A657T: 0.70) (Fig. 4*F*,*G*), highlighting that the animal's activity was directly related to the expression of cFos in each genotype but was elevated in A657T mice.

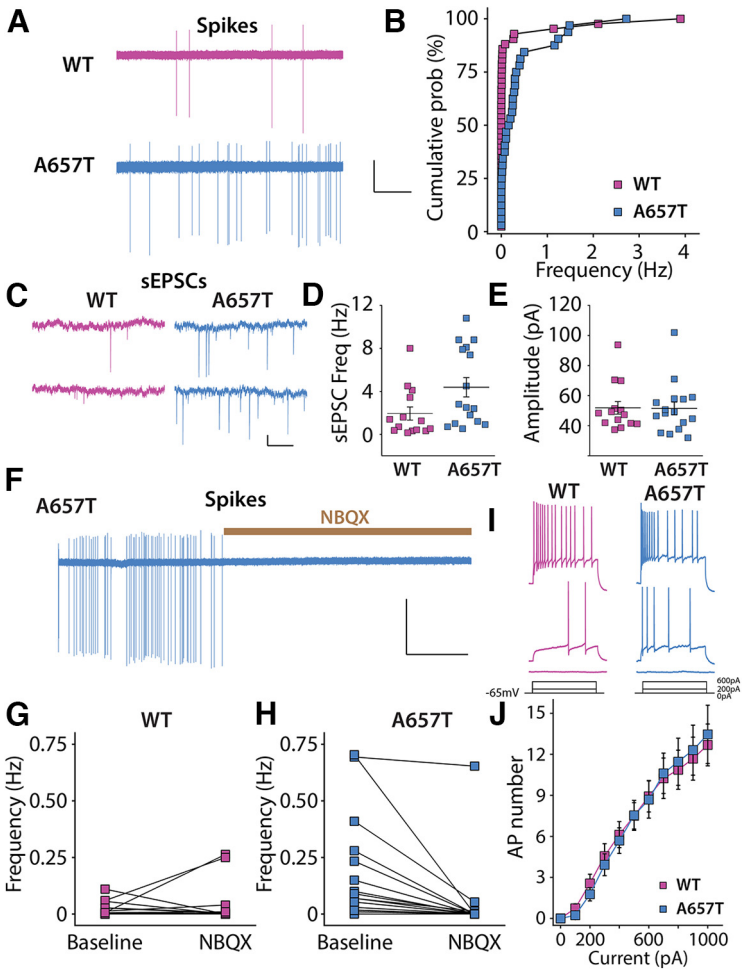

Figure 3. CA3 neurons are more excitable because of synaptic mechanisms in A657T mice. ***A***, Representative action currents (spikes) recorded from CA3 neurons in cell-attached mode from WT and A657T mice. Calibration: 50 pA, 25 s. ***B***, Cumulative distribution of spike frequency recorded in CA3 neuron from WT and A657T mice. There is an increase in spike firing in A657T mice. ***C***, Example traces of sEPSCs recorded in CA3 neurons in WT and A657T mice. Calibration: 50 pA, 1 s. ***D***, sEPSC frequency in CA3 is elevated in A657T mice. ***E***, Amplitude of sEPSCs is not affected in A657T mice. ***F***, Example continuous trace of spikes recorded in CA3 neurons prior to and after glutamate receptor antagonist application NBQX (50 μm). ***G***, Analysis of spontaneous action current frequencies before and after NBQX in WT and (***H***) A657T mice. ***I***, Example traces of APs in CA3 neurons initiated by somatic current injection. ***J***, Full frequency I-O curve for AP firing of CA3 neurons with increasing current injection.

EPSP integration and NMDAR-dependent LTP in distal AC synapses are elevated in A657T mice

Our findings demonstrate that neurons in the CA3 region are more active in A657T mice but exhibit only modest changes in their intrinsic properties, suggesting that synaptic mechanisms may play an important role in this hyperexcitability phenotype. We next tested the possibility that CA3 dendritic excitability is elevated in A657T mice, which could enhance the integration and propagation of depolarizing input in distal dendrites. We first determined whether spike coupling of AC EPSPs in the *stratum radiatum* was enhanced in A657T mice using minimal stimulation criteria (see Materials and Methods) of the stratum radiatum to evoke four AC EPSPs at 20 Hz. The evoked train of EPSPs (AC1-4) produced a significantly higher spike probability during the train in A657T mice than in WT mice (AC1-4 WT: 26.8 ± 12.6%, $n = 19$ cells, 7 mice; AC1-4 A657T: 44.4 ± 20.2%, $n = 13$ cells, 6 mice; $p = 0.039$; Mann–Whitney) (Fig. 5*A–C*). These data are consistent with a generalized increase in dendritic excitability elevating the probability that AC-CA3 synaptic input elicits an AP in CA3 neurons from A657T mice.

We next tested whether EPSP-AP coupling of MF synapses was similarly increased in A657T mice. These synapses are proximal to the soma; therefore, changes to dendritic excitability seem less likely to have the same impact on spike coupling as with AC synapses. However, the slowed kinetics of the synaptic KARs at MF synapses (Fig. 1*I*) could affect summation of these inputs in CA3 and produce an analogous change in coupling to AP initiation (Sachidhanandam et al., 2009; Pinheiro et al., 2013). We repeated the experiment using minimal stimulation of MF EPSPs to evoke a train of four MF EPSPs at 20 Hz. We found that the AP probability was not different between the two genotypes (MF1-4 WT: $n = 18$ cells, 11 mice; MF1-4 A657T: $n = 9$ cells, 7 mice; $p = 0.35$-1.0 for each bin; Mann–Whitney) (Fig. 5*D–F*). These observations are consistent with spike coupling of proximal MF synapses not being influenced by dendritic properties and with prior work suggesting that EPSP-spike coupling in MF is primarily dependent on the large presynaptic dynamics of facilitation of the synapse (Pinheiro et al., 2013), which are not affected in A657T mice (Fig. 2*A–D*).

The induction of Hebbian synaptic potentiation of distal synapses is affected by active conductances in the dendritic compartment (Magee and Johnston, 1997; Watanabe et al., 2002; Eom et al., 2022). As there appeared to be a change in the dendritic properties of CA3 neurons in A657T mice, we next tested the prediction that the threshold for NMDAR-dependent LTP of AC synapses is reduced by inducing plasticity with a submaximal

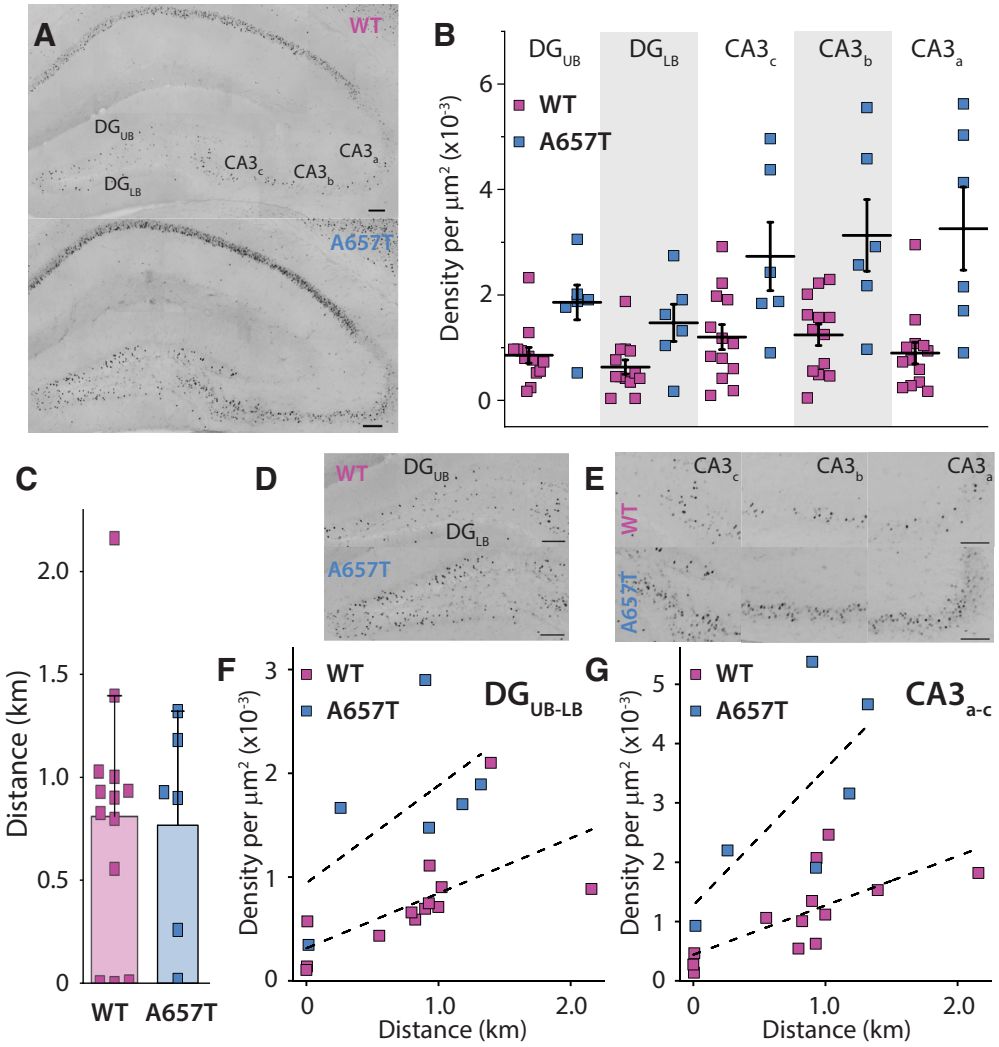

Figure 4. Neuronal activity reporter cFos is elevated in hippocampal neurons in A657T. ***A***, Representative images of the hippocampus after a single bout of running labeled with cFos from WT mice and A657T mice. Both example mice had run equivalent distances (WT: 0.898 km; A657T: 0.928 km). Calibration: 100 mm. ***B***, cFos cell density was measured in the upper and lower blade of the DG (DG_{UB}, DG_{LB}) and in each of the subregions of the CA3 a-c. ***C***, Total running distance of each animal. ***D***, Density of cFos-labeled cells in DG and (***E***) each subregion of the hippocampus in WT and A657T mice. ***F***, Total density of cFos-labeled cells of WT and A657T mice as a function of their running distance in the DG and (***G***) CA3 regions.

train of stimuli. We recorded AC fEPSPs and induced LTP using a burst of four stimuli at 50 Hz with each burst repeated 10 times every second. Consistent with a previous study (Kobayashi and Poo, 2004), this induction protocol produced a small potentiation in slices from WT mice at 35-45 min after induction (112.1 ± 9.3%, $n = 13$ cells, 6 mice) (Fig. 5*G–I*). In contrast, the same stimulation strongly potentiated AC fEPSPs in A657T mice (153.1 ± 15.0%, $n = 15$ cells, 7 mice, $p = 0.033$; Mann–Whitney) (Fig. 5*G–I*). These results suggest that the increased excitability of CA3 neurons, and particularly a potential change in the properties of active dendrites, increases the propensity for Hebbian plasticity of AC synapses in A657T mice.

CA3 neuron dendritic excitability is increased in A657T mice

Enhanced EPSP-AP coupling of distal AC synapses and a reduced threshold for the induction of NMDAR-dependent LTP suggests that dendritic excitability is enhanced in CA3 neurons in A657T mice. As an alternate measure of dendritic excitability, we determined the ability of bAPs to invade the dendrites of CA3 neurons using 2PLSM Ca^{2+} imaging. Neurons were loaded with the Ca^{2+} dye Fluo-4 (200 μM) through the patch electrode, and bAPs were evoked by somatic depolarization (Fig. 6*A–D*). The bAP-evoked Ca^{2+} signal demonstrated a decremental amplitude at more somatically distal regions of the dendrites (Fig. 6*A–F*); but in most recordings, the Ca^{2+} signal could be detected at least 250-300 µm from the soma. A comparison of the decay of the Ca^{2+} signal as a function of the distance from the soma demonstrated that there was less decrement in the signal in recordings from CA3 neurons in the A657T mice (distance constant λ; WT: $7.71 \pm 0.75 \times 10^{-3}$, $n = 17$ cells, 8 mice; A657T: $4.93 \pm 0.61 \times 10^{-3}$, $n = 15$ cells, 6 mice; $p = 0.033$; Mann–Whitney) (Fig. 6*G*). These results support the conclusion that CA3 neurons in the A657T mice have increased dendritic excitability facilitating the propagation of distal synaptic inputs (and bAPs), which contribute to the enhanced spike transmission and reduced threshold for LTP of AC synapses in CA3 neurons.

SK channels underlie the enhanced dendritic excitability and EPSP-spike coupling in A657T mice

A number of K^+ conductances can limit AP firing and affect dendritic integration of synaptic currents (Johnston et al., 2000). As we had found that dendritic excitability was enhanced in

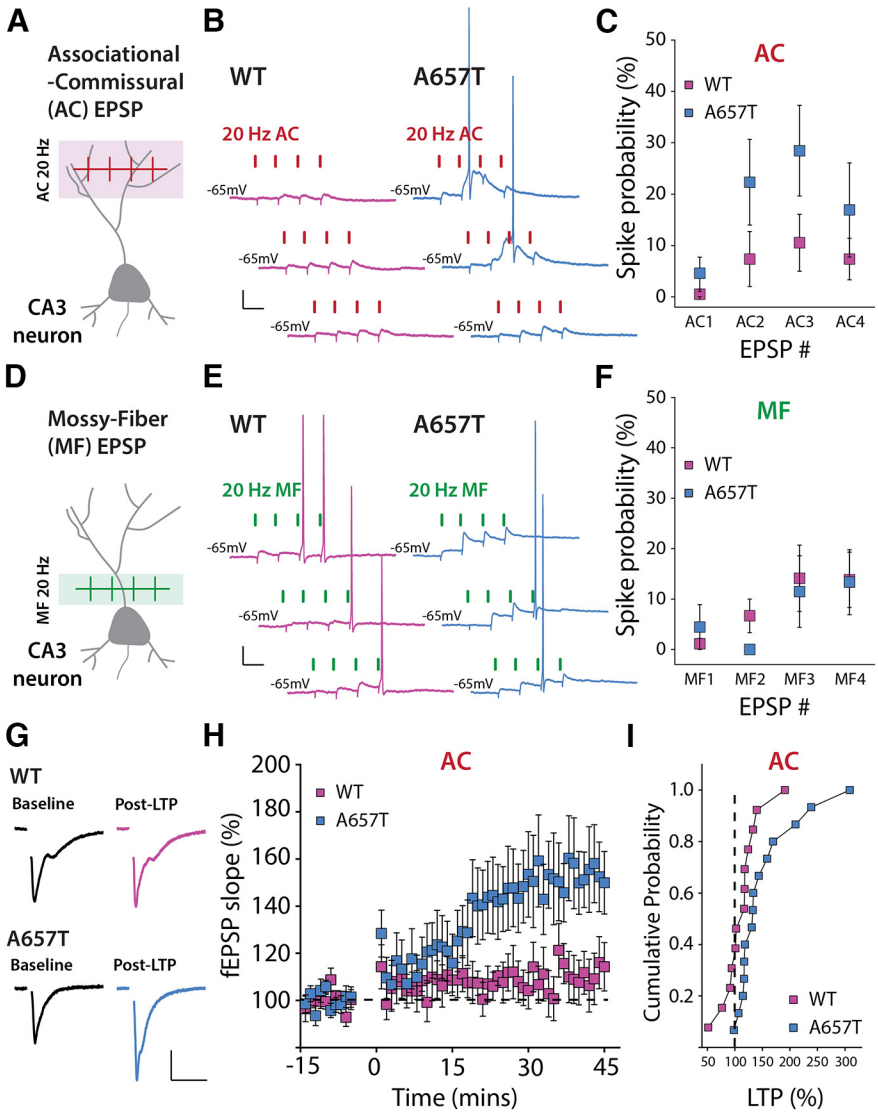

Figure 5. EPSP-spike coupling and NMDAR-dependent LTP of distal AC synapses is enhanced in A657T mice. ***A***, Diagram representation of AC-EPSP stimulation. ***B***, Representative traces of AC-EPSPs and APs stimulated at 20 Hz in CA3 neurons in WT and A657T mice. Calibration: 10 mV, 50 ms. ***C***, Spike probability at each AC-EPSP during the train of stimuli in recordings from WT and A657T mice. ***D***, Schematic of MF synaptic stimulation. ***E***, Representative MF-EPSPs and APs stimulated at 20 Hz in CA3 neurons. Calibration: 10 mV, 50 ms. ***F***, Spike probability at each MF EPSP during the 20 Hz train in WT and A657T mice. ***G***, Example traces of fEPSPs before (Baseline) and after (Post-LTP) LTP induction in WT (top) and A657T mice (bottom). Calibration: 0.2 mV, 20 ms. ***H***, Time course of LTP of AC fEPSP responses induced at time = 0 using a 4 × 50 Hz burst repeated 10 times at 1 Hz in WT and A657T mice. ***I***, Cumulative distribution for AC LTP in WT and A657T mice.

A657T mice, we focused on K^+ conductances that mediate the AHP, in particular, because this conductance can be inhibited acutely by KAR activation (Melyan et al., 2002; Fisahn et al., 2005), and some of the underlying channels are located in dendrites (Cai et al., 2004; Maher and Westbrook, 2005). The AHP can be measured in the soma following a burst of APs and is composed by mAHP and sAHP components based on the time course of the potentials. We first measured the somatic AHPs in current-clamp recordings (Fig. 7*A*,*B*). There was a significant reduction in the medium component (WT: $n = 16$ cells, 6 mice; A657T: $n = 13$ cells, 5 mice; two-way ANOVA, $F_{(1,27)} = 5.12$, $p = 0.032$) and the slow component (WT: $n = 16$ cells, 6 mice; A657T: $n = 13$ cells, 5 mice; two-way ANOVA, $F_{(1,27)} = 6.96$, $p = 0.014$) (Fig. 7*B*) of the AHPs in A657T mice. To confirm that the current underlying the AHP was indeed affected in A657T mice, we made voltage-clamp recordings and measured the somatic membrane current, I_{sAHP}, which was significantly reduced in A657T mice compared with WT mice (WT: $n = 16$ cells, 5 mice; A657T: $n = 9$ cells, 2 mice; two-way ANOVA, $F_{(1,23)} = 9.50$, $p = 0.0053$) (Fig. 7*C*,*D*). To test whether acute activation of KARs still inhibited the AHP (Melyan et al., 2002; Fisahn et al., 2005) in mutant mice, we tested whether a low concentration of the KAR agonist kainate (50 nM) inhibited both I_{mAHP} and I_{sAHP}. The magnitude of the inhibition was not different between genotypes (I_{mAHP}; WT: $11.7 \pm 2.9\%$, $n = 15$ cells, 4 mice; A657T: $32.3 \pm 13.2\%$, $n = 13$ cells, 4 mice; $p = 0.34$; Mann–Whitney; I_{sAHP}; WT: $26.9 \pm 3.9\%$, $n = 15$ cells, 4 mice; A657T: $17.0 \pm 9.4\%$, $n = 13$ cells, 4 mice; $p = 0.088$; Mann–Whitney), demonstrating that there is no change in this regulation in the A657T mice.

While there remains some uncertainty about the exact composition of the channels mediating AHPs (Adelman et al., 2012; Wang et al., 2016), prior work has demonstrated that the medium and slow AHPs are mediated by Ca^{2+}-activated K^+ channels (SK) in some neurons (Kato et al., 2006; Lee et al., 2010), including those in the hippocampus (Pedarzani et al., 2005). SK channels are localized to both soma and dendrites of hippocampal pyramidal

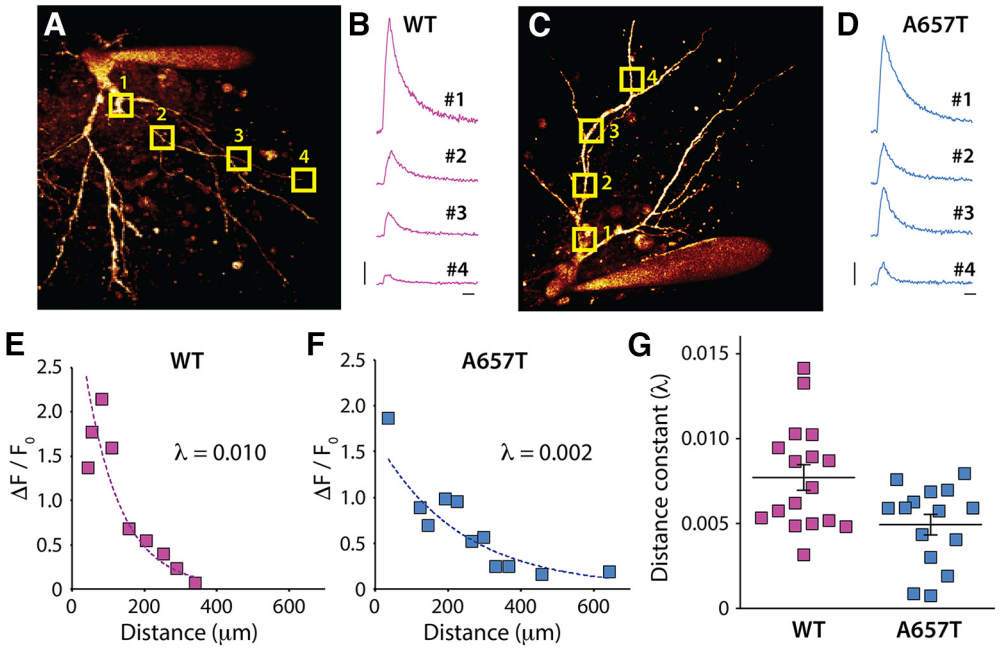

Figure 6. bAP evoked dendritic Ca^{2+} signal decays less in A657T mice. ***A***, 2PLSM image of the soma and dendrites of a CA3 neuron in slices from WT mice filled with AlexaFluor-568 through the patch electrode. Square boxes represent ROIs as regions of scan sites for AP evoked Ca^{2+} measurement. ***B***, Example fluorescence transients measured at ROIs in CA3 neurons in WT mice. ***C***, Image of a CA3 neuron from A657T mice. ***D***, Fluorescence transients measured at ROIs after somatic depolarization induced APs in A657T mice. ***B***, ***D***, Calibration: 0.25 arbitrary unit (AU), 50 ms. ***E***, Example recording from a CA3 neuron in WT mice plotting the measured amplitude of Ca^{2+} signal to the distance from soma of the scanning site fit with exponential (see Materials and Methods). Inset, Time constant of the decay (λ). ***F***, Example recording from experiment from A657T mice. Inset, Time constant of the decay (λ). ***G***, Grouped data from all recordings of measured distance constant, λ from exponential fits of dendritic Ca^{2+} evoked by APs in WT and A657T mice.

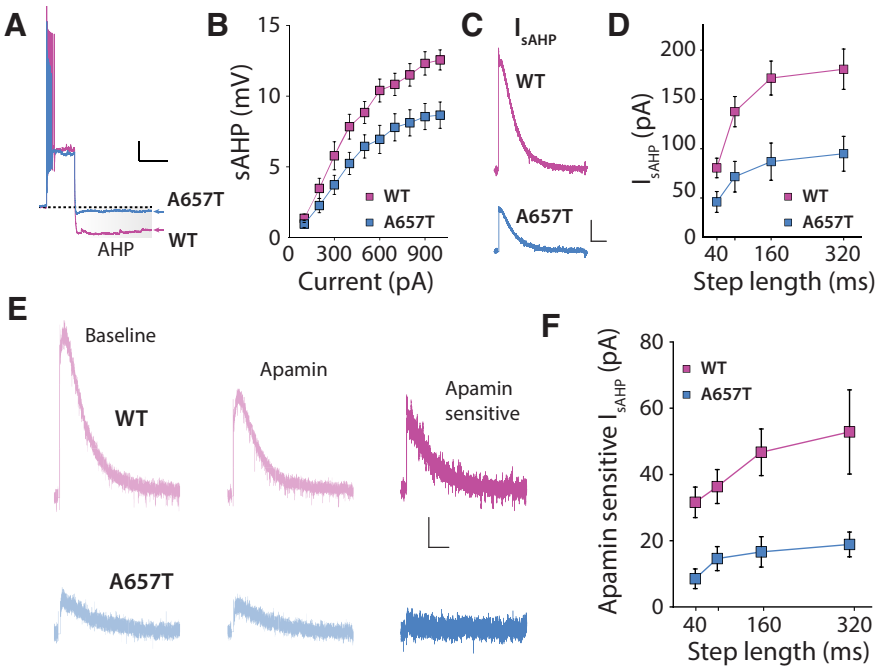

Figure 7. sAHP and SK-mediated components of the I_{sAHP} are reduced in A657T mice. ***A***, Example voltage responses to suprathreshold current steps in CA3 neurons from WT and A647T mice. The post-burst AHP (highlighted) is reduced in A657T mice. Calibration: 10 mV, 500 ms. ***B***, I-O curve for sAHP measured with increasing current injection in WT and A657T mice. ***C***, Representative currents (I_{AHP}) elicited by depolarization in CA3 neurons. Calibration: 50 pA, 2.5 s. ***D***, Amplitude of I_{sAHP} in CA3 neurons measured with increasing lengths of current injection in WT and A657T mice. ***E***, Example traces of I_{sAHP} induced by 160 ms step in CA3 neurons during baseline, application of apamin (300 nM), and the subtracted trace of the apamin-sensitive SK-mediated component from WT mice (top) and A657T mice (bottom). Calibration: 25 pA, 2.5 s. ***F***, Analysis of amplitude of apamin-sensitive component of the I_{sAHP} in CA3 neurons of WT and A657T mice.

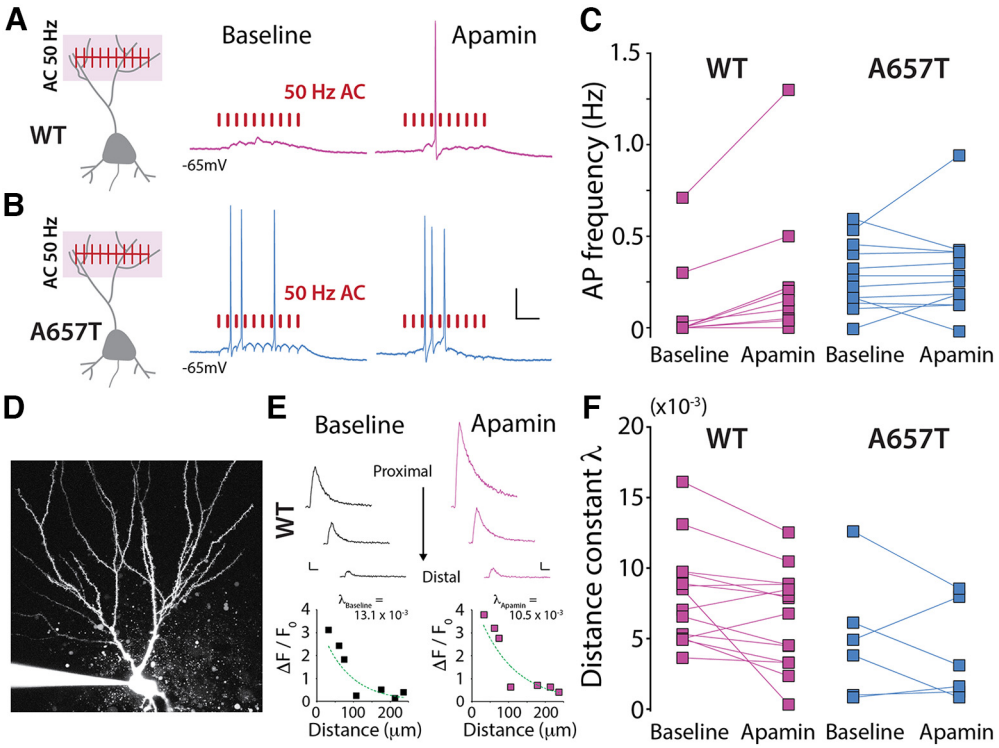

Figure 8. SK channel inhibition elevates spike coupling of AC-EPSPs and bAP evoked dendritic Ca^{2+} signals in WT mice. ***A***, Diagram representation of train stimulation of AC EPSPs and example traces during baseline and apamin (300 nM) application in WT mice and (***B***) A657T mice. Calibration: 20 mV, 50 ms. ***C***, Frequency of APs during AC-EPSP train before and after apamin application. ***D***, Example image of the soma and apical dendrites of a CA3 neuron filled with AlexaFluor-568 through the patch electrode. ***E***, Example Ca^{2+} transients measured in the dendrites of WT neuron (top) and all measurements at ROIs at different distances from soma (bottom) during baseline (left) and after apamin application (right). Calibration: 0.25 AU, 50 ms. ***F***, Distance constant (λ) calculated from fit of dendritic Ca^{2+} signals (see Materials and Methods) measured after evoked APs before and after apamin application in CA3 neurons.

neurons (Sailer et al., 2002), can limit local synaptic depolarizations in CA1 dendrites (Cai et al., 2004; Gu et al., 2008; Bock and Stuart, 2016), and constrain NMDAR-dependent LTP in CA1 Schaffer collateral synapses (Stackman et al., 2002; Hammond et al., 2006). We first examined whether the somatically recorded I_{AHP} in CA3 neurons was sensitive to SK channel blockade. Application of apamin (300 nM) significantly inhibited the I_{sAHP} in CA3 neurons in WT mice, demonstrating that a component of the I_{sAHP} in CA3 is mediated by SK (Fig. 7*E*,*F*). The sensitivity to apamin of the I_{sAHP} was significantly diminished consistent with a reduction in the SK contribution to this current in A657T mice (apamin-sensitive I_{sAHP}; WT: $n = 19$ cells, 7 mice; A657T: $n = 13$ cells, 5 mice; two-way ANOVA, $F_{(1,30)} = 10.39$, $p = 0.0030$) (Fig. 7*E*,*F*). A similar reduction in apamin sensitivity was observed in recording of I_{mAHP} (apamin-sensitive I_{mAHP}; WT: $n = 19$ cells, 7 mice; A657T: $n = 13$ cells, 5 mice; two-way ANOVA, $F_{(1,30)} = 9.97$, $p = 0.0036$). These results indicate that SK channels are major constituents of the conductances that underlie the slow and medium components of the somatic I_{AHP} in CA3 neurons and that activity of this K^+ channel is significantly diminished in CA3 neurons in A657T mice.

Prior work in CA1 neurons has demonstrated that SK channels in the dendrites are directly responsible for repolarization of glutamate receptor-evoked local dendritic plateau potentials, thereby dampening their propagation (Cai et al., 2004). Therefore, we hypothesized that reduced SK channel activity in CA3 dendrites in A657T mice could be directly responsible for the enhanced propagation of signals from distal synapses. We repeated the spike coupling experiments and tested whether inhibiting the activity of SK channels affected AC-EPSP spike coupling probability. In WT mice, acute application of apamin enhanced the probability of spike transmission after AC synaptic stimulation of 10 minimally evoked EPSPs during a 50 Hz train (WT baseline: 0.12 ± 0.08 Hz; WT apamin: 0.28 ± 0.14 Hz; $n = 9$ cells, 4 mice; $p = 0.0078$; Wilcoxon) (Fig. 8*A*,*C*). Thus, inhibiting SK channels mimicked the increased EPSP-spike coupling phenotype observed in A657T mice. In similar recordings from CA3 neurons in A657T mice, we confirmed that spike probability was enhanced, as we had observed previously, and found that apamin had no detectable effect on AC EPSP-spike coupling (A657T baseline: 0.40 ± 0.01 Hz; apamin: 0.42 ± 0.38 Hz; $n = 12$ cells, 8 mice; $p = 0.53$; Wilcoxon) (Fig. 8*B*,*C*). This occlusion of apamin's effect is consistent with the diminution of SK channel activity in dendrites of CA3 neurons contributing to the observed increase in EPSP-spike coupling of distal AC synapses in A657T mice.

To further assess how SK channel activity affects CA3 dendritic excitability, we examined whether apamin affected bAP propagation in CA3 dendrites using 2PLSM Ca^{2+} imaging. In experiments in CA3 neurons from WT animals, the decrement of the Ca^{2+} signal along the dendrite was reduced after apamin treatment in the majority of recordings (11 of 14 neurons) ($\lambda_{baseline}$: $8.02 \pm 0.93 \times 10^{-3}$; λ_{apamin}: $6.45 \pm 0.92 \times 10^{-3}$; $n = 14$ cells, 8 mice; $p = 0.017$; Wilcoxon) (Fig. 8*D*–*F*). This demonstrates that bAP propagation is facilitated in the dendrites of CA3 neurons in the presence of SK channel inhibitor and underlines an important role for SK channels in dampening CA3 dendritic excitability. When we recorded Ca^{2+} signals in CA3 neurons from A657T mice, we again found that, under control conditions, bAP propagation was enhanced (distance constant λ was reduced); but in this case, SK inhibition with apamin had no detectable effect on bAP propagation ($\lambda_{baseline}$: $5.60 \pm 1.77 \times 10^{-3}$; λ_{apamin}: $4.60 \pm 1.42 \times 10^{-3}$, $n = 6$

cells, 3 mice; $p = 0.69$; Wilcoxon). We also determined whether other conductances that affect dendritic excitability were similarly disrupted in A657T mice. Examination of the K^+ A-current (I_A), which is known to affect dendritic excitability of CA1 neurons (Kim et al., 2007), demonstrated that there was no significant change in this conductance in A657T mice (WT: $96.0 \pm 1.4\%$, $n = 16$ cells, 5 mice; A657T: $94.8 \pm 0.7\%$, $n = 14$ cells, 5 mice, $p = 0.82$, Mann–Whitney). Together, these results demonstrate that the function of SK channels that are normally required to dampen dendritic excitability in CA3 neurons is reduced or absent in the mutant A657T mice and thus contributes to enhanced dendritic excitability that affects the integration of synaptic signals and the induction of LTP in AC synapses.

Discussion

A657T mutation in GluK2 receptor affects dendritic excitability through a downregulation of SK channel function

We have discovered a surprising cellular and synaptic pathophysiology caused by the introduction of a disease-causing missense mutation in the *Grik2* gene. The most prominent finding is that dendritic excitability is increased through downregulated SK channel function in KAR mutant CA3 neurons. The modulatory activity of KARs on AHPs in hippocampal neurons has been explored over many years (Cherubini et al., 1990; Melyan et al., 2002; Fisahn et al., 2005). For example, *in vitro* recordings in CA3 neurons demonstrated that induction of LTD of KARs relieves activity-dependent inhibition of I_{sAHP}, thus reducing neuronal excitability and supporting the idea that I_{sAHP} is tonically modulated by KARs (Chamberlain et al., 2013). KARs therefore provide a feedback mechanism linking the activity of iGluRs to neuronal excitability through the K^+ conductances that underlie AHPs. This dysregulation might be because of a constitutive inhibition by tonically activated mutant KARs in CA3 neurons. These same channels in many instances play a significant role in regulating dendritic excitability. The relevance of this interplay between synaptic and intrinsic conductances to hippocampal circuits *in vivo* remains unclear because prior evidence for this modulatory activity was limited to *in vitro* studies. Here, while assessing the effect of a missense mutation that affects gating of GluK2-containing receptors in a newly developed mouse model, we unexpectedly found that CA3 neurons were more active in slices from A657T mice.

While this activity could in principle be because of an elevated intrinsic propensity for spiking, our findings suggest that the elevations in AP frequencies are synaptically driven. Intrinsic excitability was not grossly altered, and the I-O curve of somatically evoked APs was normal. In contrast, there was a clear elevation in the probability of EPSP-spike coupling in distal synapses and in AP dendritic backpropagation. A likely scenario, therefore, is that the observed elevation in neuronal activity occurs because synaptic integration is enhanced by an increase in dendritic excitability in A657T mice. This interpretation was supported by experiments in which SK channel block replicated the phenotype in WT neurons but had little effect in A657T animals. The lack of an obvious effect of apamin treatment in A657T mice was likely because of the existing diminished SK component. Thus, our findings demonstrate that SK channel function is decreased, which enhances dendritic integration and results in more active CA3 neurons in A657T mice.

The excitability of dendrites of hippocampal and cortical neurons is regulated by the localization and activity of several voltage-gated and voltage-independent ion channels that impact the propagation of synaptic depolarizations (Hoffman et al., 1997; Cai et al., 2004; Day et al., 2005; Kim et al., 2007). Small-conductance Ca^{2+} activated channels have been immunohistochemically localized to dendrites of many neuron types, including CA3 pyramidal neurons in the hippocampus (Sailer et al., 2002, 2004). Moreover, in CA1 neurons, SK channels are active in distal dendrites and limit the spread of synaptic depolarizations (Cai et al., 2004). However, decreased SK-mediated conductance and an associated increase in excitability of dendrites that elevated EPSP-AP coupling in A657T mice were unexpected. While we have not fully elucidated how this K^+ channel dysregulation is manifested, we uncover an unexpected cellular phenotype that could have a profound effect on circuit function beyond a kinetic change in synaptic KARs that makes a relatively modest postsynaptic contribution in CA3 synapses. For instance, SK channel inhibition increases the power of γ oscillations in the CA3 (Klemz et al., 2021), which could have significant effects on cognition (Mably and Colgin, 2018).

SK channels can also limit synaptic plasticity induction. Apamin blockade of SK channels reduces the threshold for NMDAR-dependent LTP in CA1 neurons (Stackman et al., 2002). We found that a relatively short induction train (Kobayashi and Poo, 2004) caused minimal potentiation (~10%) in slices from WT animals but an exaggerated potentiation (~50%) in A657T mice. These results suggest that, as in CA1 neurons (Behnisch and Reymann, 1998; Stackman et al., 2002; Hammond et al., 2006), SK channels localized to dendrites and spines act as a brake to limit LTP of distal CA3 AC synapses, the regulation of which is lost in A657T mice. Hippocampal LTP is intimately linked with memory formation, and any perturbation of memory processes is likely to have behavioral consequences by disrupting cognition. While we do not report on behavior analysis of A657T mice in this study, we measured expression of the immediate early gene cFos as an *in vivo* proxy for the activity of neurons, providing a snapshot of the relative amount of activity. We found that cFos expression was elevated in all hippocampal subregions in A657T mice, providing strong support for the conclusion that neurons are more easily activated *in vivo* in these animals.

Dendritic excitability and neurodevelopmental disorders

An emerging theme in establishing the cellular correlates of circuit dysfunction in models of neurodevelopmental disorders has focused on synaptic mechanisms, including receptors, scaffolds, and cell adhesion molecules that have been directly implicated in disease (Lerma and Marques, 2013; Yuan et al., 2015; Vieira et al., 2021). These synaptic deficits in many cases are primary causes of changes in the balance of excitatory and inhibitory synaptic transmission which are associated with many neurodevelopmental and neuropsychiatric disorders (Sohal and Rubenstein, 2019). Similarly, there are numerous channelopathies that are caused by variants in both voltage-gated and Ca^{2+}-gated ion channels (Park et al., 2019; Miller et al., 2021). Despite this, there are only a few examples of studies that have directly assessed dendritic mechanisms in mouse models of NDDs and yet fewer studies in which dendritic excitability has been characterized in detail. As one example, autism spectrum disorder can result from loss-of-function mutations in the *SCN2A* gene, which encoded the Nav1.2 sodium channel (Sanders et al., 2012). *Scn2A* haploinsufficiency in mice causes a reduction in excitability of the dendritic compartment of cortical pyramidal cell dendrites, reducing bAPs

and synaptic plasticity (Spratt et al., 2019). In the *Fmr1* KO mouse, the model of fragile X syndrome, multiple ion channels have been reported to be disrupted; and in CA1 neurons, a specific loss of dendritic Kv4 elevated the excitability of the dendritic compartment, increased propagation of bAPs, and enhanced synaptic plasticity (Routh et al., 2013). These studies demonstrate that either direct or indirect loss of voltage-dependent channels in the dendritic compartment can affect dendritic computations in mouse models of NDD.

In our study, a missense mutation in the gene encoding the glutamate gated receptor subunit GluK2 revealed a functional coupling *in vivo* to SK channels that regulate dendritic excitability. The relevance of KAR modulation of AHPs to brain function has been a mystery; therefore, this study provides evidence that this functional coupling could play a significant role in the normal physiological properties of CA3 neurons. Aberrant SK activity has also been described in other NDD mouse models. Haploinsufficient *Pten* mice, another autism spectrum disorder model, have a marked increase in SK function in L2/3 cortical neurons, causing a decrease in excitability but not affecting dendritic integration of subthreshold synaptic events (Garcia-Junco-Clemente et al., 2013). In *Fmr1* KO mice, it was recently demonstrated that SK currents are reduced in CA3 neurons because of a loss of a direct protein interaction between Fmrp and SK2 causing elevated neuronal excitability (Deng et al., 2019). It remains to be tested whether CA3 dendritic excitability and synaptic integration are affected in *Fmr1* KO mice similar to what we have observed in the A657T mice. Conversely, loss of *Ube3a* ubiquitination of SK2 in the mouse model of Angelman syndrome results in increased spine expression of SK2 in CA1 neurons and impairs LTP induction (Sun et al., 2015). Thus, there is a growing appreciation that SK dysfunction in mouse models of NDDs can disrupt excitability and synaptic plasticity mechanisms. The importance of SK to normal brain development and function is further highlighted by the recent discovery of *de novo* and inherited loss-of-function variants in *KCNN2*, which encodes the SK2 channel, in patients with delays in motor, intellectual, and language development (Mochel et al., 2020). These phenotypes in SK2 disorders overlap with the clinical phenotype observed in the individuals carrying the A657T mutation in *GRIK2* gene (Guzman et al., 2017; Stolz et al., 2021).

The mechanistic basis for alterations in K^+ channel activity and dendritic excitability caused by this particular *Grik2* mutation is not clear. Unfortunately, our proteomic analysis did not detect Kcnn2 peptides (SK2 channel), which is often the case for low expression proteins; thus, other methodologies will be required for future assessment of SK channel expression and localization. These effects on SK are likely in part pleiotropic because of developmental consequences that cannot be extricated from their acute effects on the phenotype. Indeed, in this case, we are modeling a neurodevelopmental disorder in humans and would expect the mutation to have effects throughout the life of the animal. We did indeed see elevated spiking of CA3 neurons in perinatal mice (P12-P15; data not shown), similar to the adult phenotype we report in the paper, suggesting that this is also prevalent when the brain is still developing. Future mechanistic studies using genetic or viral tools to conditionally express or knockdown mutant receptors could shed further light on these questions.

There is a growing list of variants in glutamate receptor genes associated with human NDDs, but it is not at all clear how those mutations cause functional alterations of neural circuits. Here we found that an orthologous single amino acid mutation in the GluK2 in a mouse had an unexpected effect on K^+ channel function and dendritic excitability. Our findings provide novel insight into how disease-causing iGluR mutations can disrupt neuronal and circuit function.

References

Adelman JP, Maylie J, Sah P (2012) Small-conductance Ca^{2+}-activated K^+ channels: form and function. Annu Rev Physiol 74:245–269.

Armstrong JN, Saganich MJ, Xu NJ, Henkemeyer M, Heinemann SF, Contractor A (2006) B-ephrin reverse signaling is required for NMDA-independent long-term potentiation of mossy fibers in the hippocampus. J Neurosci 26:3474–3481.

Barthet G, Moreira-de-Sa A, Zhang P, Deforges S, Castanheira J, Gorlewicz A, Mulle C (2022) Presenilin and APP regulate synaptic kainate receptors. J Neurosci 42:9253–9262.

Behnisch T, Reymann KG (1998) Inhibition of apamin-sensitive calcium dependent potassium channels facilitate the induction of long-term potentiation in the CA1 region of rat hippocampus in vitro. Neurosci Lett 253:91–94.

Bock T, Stuart GJ (2016) Impact of calcium-activated potassium channels on NMDA spikes in cortical layer 5 pyramidal neurons. J Neurophysiol 115:1740–1748.

Burnashev N, Szepetowski P (2015) NMDA receptor subunit mutations in neurodevelopmental disorders. Curr Opin Pharmacol 20:73–82.

Cai X, Liang CW, Muralidharan S, Kao JP, Tang CM, Thompson SM (2004) Unique roles of SK and Kv4.2 potassium channels in dendritic integration. Neuron 44:351–364.

Castillo PE, Malenka RC, Nicoll RA (1997) Kainate receptors mediate a slow postsynaptic current in hippocampal CA3 neurons. Nature 388:182–186.

Chamberlain SE, Sadowski JH, Teles-Grilo Ruivo LM, Atherton LA, Mellor JR (2013) Long-term depression of synaptic kainate receptors reduces excitability by relieving inhibition of the slow afterhyperpolarization. J Neurosci 33:9536–9545.

Chatzi C, Zhang Y, Hendricks WD, Chen Y, Schnell E, Goodman RH, Westbrook GL (2019) Exercise-induced enhancement of synaptic function triggered by the inverse BAR protein, Mtss1L. Elife 8:e45920.

Chen X, Yuan LL, Zhao C, Birnbaum SG, Frick A, Jung WE, Schwarz TL, Sweatt JD, Johnston D (2006) Deletion of Kv4.2 gene eliminates dendritic A-type K^+ current and enhances induction of long-term potentiation in hippocampal CA1 pyramidal neurons. J Neurosci 26:12143–12151.

Cherubini E, Rovira C, Ben-Ari Y, Nistri A (1990) Effects of kainate on the excitability of rat hippocampal neurones. Epilepsy Res 5:18–27.

Cociorva D, Tabb DL, Yates JR (2007) Validation of tandem mass spectrometry database search results using DTASelect. Curr Protoc Bioinformatics Chapter 13:Unit 13.4.

Cohen I, Miles R (2000) Contributions of intrinsic and synaptic activities to the generation of neuronal discharges in in vitro hippocampus. J Physiol 524:485–502.

Contractor A, Swanson GT, Sailer A, O'Gorman S, Heinemann SF (2000) Identification of the kainate receptor subunits underlying modulation of excitatory synaptic transmission in the CA3 region of the hippocampus. J Neurosci 20:8269–8278.

Contractor A, Swanson G, Heinemann SF (2001) Kainate receptors are involved in short- and long-term plasticity at mossy fiber synapses in the hippocampus. Neuron 29:209–216.

Coombs ID, Ziobro J, Krotov V, Surtees TL, Cull-Candy SG, Farrant M (2022) A gain-of-function GRIA2 variant associated with neurodevelopmental delay and seizures: functional characterization and targeted treatment. Epilepsia 63:e156–e163.

Coutelier M, Burglen L, Mundwiller E, Abada-Bendib M, Rodriguez D, Chantot-Bastaraud S, Rougeot C, Cournelle MA, Milh M, Toutain A, Bacq D, Meyer V, Afenjar A, Deleuze JF, Brice A, Heron D, Stevanin G, Durr A (2015) GRID2 mutations span from congenital to mild adult-onset cerebellar ataxia. Neurology 84:1751–1759.

Davies B, et al., WGS500 Consortium (2017) A point mutation in the ion conduction pore of AMPA receptor GRIA3 causes dramatically perturbed sleep patterns as well as intellectual disability. Hum Mol Genet 26:3869–3882.

Day M, Carr DB, Ulrich S, Ilijic E, Tkatch T, Surmeier DJ (2005) Dendritic excitability of mouse frontal cortex pyramidal neurons is shaped by the

interaction among HCN, Kir2, and Kleak channels. J Neurosci 25:8776–8787.
Day M, Wokosin D, Plotkin JL, Tian X, Surmeier DJ (2008) Differential excitability and modulation of striatal medium spiny neuron dendrites. J Neurosci 28:11603–11614.
Deng PY, Carlin D, Oh YM, Myrick LK, Warren ST, Cavalli V, Klyachko VA (2019) Voltage-independent SK-channel dysfunction causes neuronal hyperexcitability in the hippocampus of Fmr1 knock-out mice. J Neurosci 39:28–43.
Eng JK, McCormack AL, Yates JR (1994) An approach to correlate tandem mass spectral data of peptides with amino acid sequences in a protein database. J Am Soc Mass Spectrom 5:976–989.
Eom K, Lee HR, Hyun JH, An H, Lee YS, Ho WK, Lee SH (2022) Gradual decorrelation of CA3 ensembles associated with contextual discrimination learning is impaired by Kv1.2 insufficiency. Hippocampus 32:193–216.
Fernandes HB, Catches JS, Petralia RS, Copits BA, Xu J, Russell TA, Swanson GT, Contractor A (2009) High-affinity kainate receptor subunits are necessary for ionotropic but not metabotropic signaling. Neuron 63:818–829.
Fisahn A, Heinemann SF, McBain CJ (2005) The kainate receptor subunit GluR6 mediates metabotropic regulation of the slow and medium AHP currents in mouse hippocampal neurones. J Physiol 562:199–203.
Garcia-Junco-Clemente P, Chow DK, Tring E, Lazaro MT, Trachtenberg JT, Golshani P (2013) Overexpression of calcium-activated potassium channels underlies cortical dysfunction in a model of PTEN-associated autism. Proc Natl Acad Sci USA 110:18297–18302.
Geisheker MR, et al. (2017) Hotspots of missense mutation identify neurodevelopmental disorder genes and functional domains. Nat Neurosci 20:1043–1051.
Gu N, Hu H, Vervaeke K, Storm JF (2008) SK (KCa2) channels do not control somatic excitability in CA1 pyramidal neurons but can be activated by dendritic excitatory synapses and regulate their impact. J Neurophysiol 100:2589–2604.
Guzman YF, Ramsey K, Stolz JR, Craig DW, Huentelman MJ, Narayanan V, Swanson GT (2017) A gain-of-function mutation in the GRIK2 gene causes neurodevelopmental deficits. Neurol Genet 3:e129.
Hammond RS, Bond CT, Strassmaier T, Ngo-Anh TJ, Adelman JP, Maylie J, Stackman RW (2006) Small-conductance Ca^{2+}-activated K^+ channel type 2 (SK2) modulates hippocampal learning, memory, and synaptic plasticity. J Neurosci 26:1844–1853.
Hoffman DA, Magee JC, Colbert CM, Johnston D (1997) K^+ channel regulation of signal propagation in dendrites of hippocampal pyramidal neurons. Nature 387:869–875.
Johnston D, Hoffman DA, Magee JC, Poolos NP, Watanabe S, Colbert CM, Migliore M (2000) Dendritic potassium channels in hippocampal pyramidal neurons. J Physiol 525:75–81.
Kato M, Tanaka N, Usui S, Sakuma Y (2006) The SK channel blocker apamin inhibits slow afterhyperpolarization currents in rat gonadotropin-releasing hormone neurones. J Physiol 574:431–442.
Kim J, Jung SC, Clemens AM, Petralia RS, Hoffman DA (2007) Regulation of dendritic excitability by activity-dependent trafficking of the A-type K^+ channel subunit Kv4.2 in hippocampal neurons. Neuron 54:933–947.
Klemz A, Wildner F, Tutuncu E, Gerevich Z (2021) Regulation of hippocampal gamma oscillations by modulation of intrinsic neuronal excitability. Front Neural Circuits 15:778022.
Kobayashi K, Poo MM (2004) Spike train timing-dependent associative modification of hippocampal CA3 recurrent synapses by mossy fibers. Neuron 41:445–454.
Lauri SE, Ryazantseva M, Orav E, Vesikansa A, Taira T (2021) Kainate receptors in the developing neuronal networks. Neuropharmacology 195:108585.
Lee K, Duan W, Sneyd J, Herbison AE (2010) Two slow calcium-activated afterhyperpolarization currents control burst firing dynamics in gonadotropin-releasing hormone neurons. J Neurosci 30:6214–6224.
Lemke JR, et al. (2016) Delineating the GRIN1 phenotypic spectrum: a distinct genetic NMDA receptor encephalopathy. Neurology 86:2171–2178.
Lerma J, Marques JM (2013) Kainate receptors in health and disease. Neuron 80:292–311.
Mably AJ, Colgin LL (2018) Gamma oscillations in cognitive disorders. Curr Opin Neurobiol 52:182–187.
Magee JC, Johnston D (1997) A synaptically controlled, associative signal for Hebbian plasticity in hippocampal neurons. Science 275:209–213.
Mahadevan V, Pressey JC, Acton BA, Uvarov P, Huang MY, Chevrier J, Puchalski A, Li CM, Ivakine EA, Airaksinen MS, Delpire E, McInnes RR, Woodin MA (2014) Kainate receptors coexist in a functional complex with KCC2 and regulate chloride homeostasis in hippocampal neurons. Cell Rep 7:1762–1770.
Maher BJ, Westbrook GL (2005) SK channel regulation of dendritic excitability and dendrodendritic inhibition in the olfactory bulb. J Neurophysiol 94:3743–3750.
Martin S, Chamberlin A, Shinde DN, Hempel M, Strom TM, Schreiber A, Johannsen J, Ousager LB, Larsen MJ, Hansen LK, Fatemi A, Cohen JS, Lemke J, Sorensen KP, Helbig KL, Lessel D, Abou Jamra R (2017) De novo variants in GRIA4 lead to intellectual disability with or without seizures and gait abnormalities. Am J Hum Genet 101:1013–1020.
McAlister GC, Nusinow DP, Jedrychowski MP, Wuhr M, Huttlin EL, Erickson BK, Rad R, Haas W, Gygi SP (2014) MultiNotch MS3 enables accurate, sensitive, and multiplexed detection of differential expression across cancer cell line proteomes. Anal Chem 86:7150–7158.
Melyan Z, Wheal HV, Lancaster B (2002) Metabotropic-mediated kainate receptor regulation of IsAHP and excitability in pyramidal cells. Neuron 34:107–114.
Miller JP, Moldenhauer HJ, Keros S, Meredith AL (2021) An emerging spectrum of variants and clinical features in KCNMA1-linked channelopathy. Channels (Austin) 15:447–464.
Mochel F, et al. (2020) Variants in the SK2 channel gene (KCNN2) lead to dominant neurodevelopmental movement disorders. Brain 143:3564–3573.
Mulle C, Sailer A, Perez-Otano I, Dickinson-Anson H, Castillo PE, Bureau I, Maron C, Gage FH, Mann JR, Bettler B, Heinemann SF (1998) Altered synaptic physiology and reduced susceptibility to kainate-induced seizures in GluR6-deficient mice. Nature 392:601–605.
Myers SJ, Yuan H, Kang JQ, Tan FC, Traynelis SF, Low CM (2019) Distinct roles of GRIN2A and GRIN2B variants in neurological conditions. F1000Res 8.
Nomura T, Musial TF, Marshall JJ, Zhu Y, Remmers CL, Xu J, Nicholson DA, Contractor A (2017) Delayed maturation of fast-spiking interneurons is rectified by activation of the TrkB receptor in the mouse model of Fragile X syndrome. J Neurosci 37:11298–11310.
Oladehin A, Waters RS (2001) Location and distribution of Fos protein expression in rat hippocampus following acute moderate aerobic exercise. Exp Brain Res 137:26–35.
Park J, et al. (2019) KCNC1-related disorders: new de novo variants expand the phenotypic spectrum. Ann Clin Transl Neurol 6:1319–1326.
Pedarzani P, McCutcheon JE, Rogge G, Jensen BS, Christophersen P, Hougaard C, Strobaek D, Stocker M (2005) Specific enhancement of SK channel activity selectively potentiates the afterhyperpolarizing current I (AHP) and modulates the firing properties of hippocampal pyramidal neurons. J Biol Chem 280:41404–41411.
Peng J, Elias JE, Thoreen CC, Licklider LJ, Gygi SP (2003) Evaluation of multidimensional chromatography coupled with tandem mass spectrometry (LC/LC-MS/MS) for large-scale protein analysis: the yeast proteome. J Proteome Res 2:43–50.
Pinheiro PS, Perrais D, Coussen F, Barhanin J, Bettler B, Mann JR, Malva JO, Heinemann SF, Mulle C (2007) GluR7 is an essential subunit of presynaptic kainate autoreceptors at hippocampal mossy fiber synapses. Proc Natl Acad Sci USA 104:12181–12186.
Pinheiro PS, Lanore F, Veran J, Artinian J, Blanchet C, Crepel V, Perrais D, Mulle C (2013) Selective block of postsynaptic kainate receptors reveals their function at hippocampal mossy fiber synapses. Cereb Cortex 23:323–331.
Platzer K, et al. (2017) GRIN2B encephalopathy: novel findings on phenotype, variant clustering, functional consequences and treatment aspects. J Med Genet 54:460–470.
Plotkin JL, Shen W, Rafalovich I, Sebel LE, Day M, Chan CS, Surmeier DJ (2013) Regulation of dendritic calcium release in striatal spiny projection neurons. J Neurophysiol 110:2325–2336.
Rodriguez-Moreno A, Lerma J (1998) Kainate receptor modulation of GABA release involves a metabotropic function. Neuron 20:1211–1218.
Routh BN, Johnston D, Brager DH (2013) Loss of functional A-type potassium channels in the dendrites of CA1 pyramidal neurons from a mouse model of fragile X syndrome. J Neurosci 33:19442–19450.

Rozas JL, Paternain AV, Lerma J (2003) Noncanonical signaling by ionotropic kainate receptors. Neuron 39:543–553.
Sachidhanandam S, Blanchet C, Jeantet Y, Cho YH, Mulle C (2009) Kainate receptors act as conditional amplifiers of spike transmission at hippocampal mossy fiber synapses. J Neurosci 29:5000–5008.
Sailer CA, Hu H, Kaufmann WA, Trieb M, Schwarzer C, Storm JF, Knaus HG (2002) Regional differences in distribution and functional expression of small-conductance Ca^{2+}-activated K^+ channels in rat brain. J Neurosci 22:9698–9707.
Sailer CA, Kaufmann WA, Marksteiner J, Knaus HG (2004) Comparative immunohistochemical distribution of three small-conductance Ca^{2+}-activated potassium channel subunits, SK1, SK2, and SK3 in mouse brain. Mol Cell Neurosci 26:458–469.
Salpietro V, et al. SYNAPS Study Group (2019) AMPA receptor GluA2 subunit defects are a cause of neurodevelopmental disorders. Nat Commun 10:3094.
Sanders SJ, et al. (2012) De novo mutations revealed by whole-exome sequencing are strongly associated with autism. Nature 485:237–241.
Schmitz D, Mellor J, Nicoll RA (2001) Presynaptic kainate receptor mediation of frequency facilitation at hippocampal mossy fiber synapses. Science 291:1972–1976.
Sohal VS, Rubenstein JL (2019) Excitation-inhibition balance as a framework for investigating mechanisms in neuropsychiatric disorders. Mol Psychiatry 24:1248–1257.
Spratt PW, Ben-Shalom R, Keeshen CM, Burke KJ Jr, Clarkson RL, Sanders SJ, Bender KJ (2019) The autism-associated gene Scn2a contributes to dendritic excitability and synaptic function in the prefrontal cortex. Neuron 103:673–685.e675.
Stackman RW, Hammond RS, Linardatos E, Gerlach A, Maylie J, Adelman JP, Tzounopoulos T (2002) Small conductance Ca^{2+}-activated K^+ channels modulate synaptic plasticity and memory encoding. J Neurosci 22:10163–10171.
Stolz JR, et al. (2021) Clustered mutations in the GRIK2 kainate receptor subunit gene underlie diverse neurodevelopmental disorders. Am J Hum Genet 108:1692–1709.
Sun J, Zhu G, Liu Y, Standley S, Ji A, Tunuguntla R, Wang Y, Claus C, Luo Y, Baudry M, Bi X (2015) UBE3A regulates synaptic plasticity and learning and memory by controlling SK2 channel endocytosis. Cell Rep 12:449–461.
Tabb DL, McDonald WH, Yates JR 3rd (2002) DTASelect and Contrast: tools for assembling and comparing protein identifications from shotgun proteomics. J Proteome Res 1:21–26.
Ting L, Rad R, Gygi SP, Haas W (2011) MS3 eliminates ratio distortion in isobaric multiplexed quantitative proteomics. Nat Methods 8:937–940.
Tsuchida R, Yamaguchi T, Funabashi D, Koumi Y, Kita I, Nishijima T (2022) Exercise type influences the effect of an acute bout of exercise on hippocampal neuronal activation in mice. Neurosci Lett 783:136707.
UniProt Consortium (2015) UniProt: a hub for protein information. Nucleic Acids Res 43:D204–D212.
Vesikansa A, Sakha P, Kuja-Panula J, Molchanova S, Rivera C, Huttunen HJ, Rauvala H, Taira T, Lauri SE (2012) Expression of GluK1c underlies the developmental switch in presynaptic kainate receptor function. Sci Rep 2:310.
Vieira MM, Jeong J, Roche KW (2021) The role of NMDA receptor and neuroligin rare variants in synaptic dysfunction underlying neurodevelopmental disorders. Curr Opin Neurobiol 69:93–104.
Vogel MW, Caston J, Yuzaki M, Mariani J (2007) The Lurcher mouse: fresh insights from an old mutant. Brain Res 1140:4–18.
Wang K, Mateos-Aparicio P, Honigsperger C, Raghuram V, Wu WW, Ridder MC, Sah P, Maylie J, Storm JF, Adelman JP (2016) IK1 channels do not contribute to the slow afterhyperpolarization in pyramidal neurons. Elife 5:e11206.
Watanabe S, Hoffman DA, Migliore M, Johnston D (2002) Dendritic K^+ channels contribute to spike-timing dependent long-term potentiation in hippocampal pyramidal neurons. Proc Natl Acad Sci USA 99:8366–8371.
Wu Y, et al. (2007) Mutations in ionotropic AMPA receptor 3 alter channel properties and are associated with moderate cognitive impairment in humans. Proc Natl Acad Sci USA 104:18163–18168.
Xu T, Park SK, Venable JD, Wohlschlegel JA, Diedrich JK, Cociorva D, Lu B, Liao L, Hewel J, Han X, Wong CC, Fonslow B, Delahunty C, Gao Y, Shah H, Yates JR 3rd (2015) ProLuCID: an improved SEQUEST-like algorithm with enhanced sensitivity and specificity. J Proteomics 129:16–24.
Yuan H, Low CM, Moody OA, Jenkins A, Traynelis SF (2015) Ionotropic GABA and glutamate receptor mutations and human neurologic diseases. Mol Pharmacol 88:203–217.
Zuo J, De Jager PL, Takahashi KA, Jiang W, Linden DJ, Heintz N (1997) Neurodegeneration in Lurcher mice caused by mutation in delta2 glutamate receptor gene. Nature 388:769–773.